OXFORD

ORIGINAL ARTICLE

Unaltered Network Activity and Interneuronal Firing During Spontaneous Cortical Dynamics In Vivo in a Mouse Model of Severe Myoclonic Epilepsy of Infancy

Angela Michela De Stasi[1,2], Pasqualina Farisello[1,3], Iacopo Marcon[4], Stefano Cavallari[2,5], Angelo Forli[1,2], Dania Vecchia[1,2], Gabriele Losi[4], Massimo Mantegazza[6], Stefano Panzeri[2,5], Giorgio Carmignoto[4], Alberto Bacci[3,7,8] and Tommaso Fellin[1,2]

[1]Optical Approaches to Brain Function Laboratory, [2]Neural Coding Laboratory, Neuroscience and Brain Technologies Department, Istituto Italiano di Tecnologia, Genova, Italy, [3]Fondazione EBRI "Rita Levi-Montalcini", Roma, Italy, [4]CNR Neuroscience Institute and University of Padova, Padova, Italy, [5]Neural Computation Laboratory, Istituto Italiano di Tecnologia, Rovereto, Italy, [6]Institute of Molecular and Cellular Pharmacology (IPMC), CNRS UMR7275 and University of Nice-Sophia Antipolis, Valbonne, France, [7]Sorbonne Universités UPMC Paris 06, UMR S 1127, Inserm U 1127, CNRS UMR 7225, Paris, France and [8]ICM—Institut du Cerveau et de la Moelle épinière, Paris, France

Address correspondence to Alberto Bacci, ICM—Institut du Cerveau et de la Moelle épinière, Paris, France. Email: alberto.bacci@icm-institute.org; Tommaso Fellin, Optical Approaches to Brain Function Laboratory and Neural Coding Laboratory, Istituto Italiano di Tecnologia, Via Morego 30, 16163 Genova, Italy. Email: tommaso.fellin@iit.it

Angela Michela De Stasi and Pasqualina Farisello equally contributed to this study.

Abstract

Severe myoclonic epilepsy of infancy (SMEI) is associated with loss of function of the *SCN1A* gene encoding the $Na_V1.1$ sodium channel isoform. Previous studies in *Scn1a*$^{-/+}$ mice during the pre-epileptic period reported selective reduction in interneuron excitability and proposed this as the main pathological mechanism underlying SMEI. Yet, the functional consequences of this interneuronal dysfunction at the circuit level in vivo are unknown. Here, we investigated whether *Scn1a*$^{-/+}$ mice showed alterations in cortical network function. We found that various forms of spontaneous network activity were similar in *Scn1a*$^{-/+}$ during the pre-epileptic period compared with wild-type (WT) in vivo. Importantly, in brain slices from *Scn1a*$^{-/+}$ mice, the excitability of parvalbumin (PV) and somatostatin (SST) interneurons was reduced, epileptiform activity propagated more rapidly, and complex synaptic changes were observed. However, in vivo, optogenetic reduction of firing in PV or SST cells in WT mice modified ongoing network activities, and juxtasomal recordings from identified PV and SST interneurons showed unaffected interneuronal firing during spontaneous cortical dynamics in *Scn1a*$^{-/+}$ compared with WT. These results demonstrate that interneuronal hypoexcitability is not observed in *Scn1a*$^{-/+}$ mice during spontaneous activities in vivo and suggest that additional mechanisms may contribute to homeostatic rearrangements and the pathogenesis of SMEI.

Introduction

Severe myoclonic epilepsy of infancy (SMEI), or Dravet syndrome, is a rare epileptic encephalopathy, characterized by severe intractable seizures, ataxia, autistic-like deficits, cognitive disorders, and premature death (Dravet 2000; Dravet et al. 2005). Many drugs are ineffective in the treatment of SMEI and currently no cure is available. Mutations in the SCN1A gene, coding for the alpha subunit of the voltage-gated sodium channels Na$_V$1.1, were identified in approximately 70% of SMEI patients (Meisler and Kearney 2005), with most mutations leading to a haploinsufficiency and loss of channel function (Claes et al. 2001; Ohmori et al. 2002). Importantly, a mouse model generated by disrupting one allele of the Scn1a gene (Scn1a$^{-/+}$ mouse) recapitulates many aspects of the human pathology, including an initial asymptomatic period followed by the appearance of temperature-induced seizures, spontaneous seizures, and sporadic death after the third postnatal week (Yu et al. 2006). Several studies investigated the pathogenic mechanisms leading to SMEI, focusing mainly on the early cellular dysfunctions that occur in the epileptogenic period. During the initial asymptomatic period, pyramidal neurons showed no differences in the voltage dependence of activation and inactivation of sodium channels in Scn1a$^{-/+}$ mice (Yu et al. 2006). Remarkably, however, both in cortical structures and in cerebellum, GABAergic inhibitory interneurons exhibited a significant decrease in voltage-dependent sodium current, leading to reduced firing (Yu et al. 2006). These data agree with immunohistological evidence suggesting preferential expression of Na$_V$1.1 in interneurons (Ogiwara et al. 2007). Therefore, understanding how functional alterations of the Na$_V$1.1 channel are reflected in cortical network changes during the pre-epileptic period is fundamental to identify possible therapeutic avenues before the onset of this devastating disease.

In cortical structures, GABAergic interneurons are remarkably heterogeneous (Ascoli et al. 2008; DeFelipe et al. 2013): Different interneuron types inhibit specific compartments of principal neurons, resulting in a highly specialized division of labor, governing all forms of cortical activity (Isaacson and Scanziani 2011). Accordingly, malfunctioning of specific GABAergic circuits often results in neurological and psychiatric symptoms (Lewis et al. 2011; Marin 2012; Le and Monyer 2013), such as those shown in SMEI patients (Dravet et al. 2005). In Scn1a$^{-/+}$ mice, the excitability of both parvalbumin- (PV) and somatostatin- (SST) positive cells is reduced (Tai et al. 2014), suggesting that an altered excitability is shared among different interneuron subtypes. Moreover, selective disruption of the Scn1a gene in PV-positive (Dutton et al. 2011) or SST-positive (Rubinstein et al. 2015) cells increased susceptibility to thermally induced seizures.

Based on these findings, it was proposed that, during the epileptogenic period, reduced excitability of specific subclasses of interneurons represents the main cellular mechanism leading to SMEI. Given the crucial role of interneurons in sculpting cortical activity (Isaacson and Scanziani 2011), disruption of interneuron excitability is expected to result in major network alterations. However, cellular studies on Scn1a mutant mice were performed in brain slices, which, although allowing in-depth analyses of excitability and synaptic properties at single-cell level, are devoid of the constant intense activity typical of the living brain. Thus, the functional consequences of Scn1a deletion and of interneuron dysfunction on neuronal networks in vivo are still unknown.

To address this issue, we combined in vivo electrophysiological recordings, optogenetics, and two-photon-guided juxtasomal recordings with patch-clamp recordings from genetically identified interneurons in brain slices from Scn1a$^{-/+}$ mice, focusing on the pre-epileptic period. Surprisingly, we found that spontaneous cortical dynamics were largely unchanged in anesthetized and awake Scn1a$^{-/+}$ animals compared with controls in vivo. Patch-clamp recordings in cortical slices confirmed PV and SST interneurons' reduced excitability upon current injections, and altered synaptic activity. However, these deficits were not paralleled by altered interneuronal firing during in vivo network activity. Importantly, acute and reversible reduction of PV- and SST-positive cell firing in control mice invariably resulted in enhanced network activity. These findings suggest that reduced interneuronal excitability in Scn1a$^{-/+}$ animals is not the only alteration occurring during the pre-epileptic period, and that additional mechanisms may play a role in homeostatic rearrangements and in the genesis of SMEI.

Materials and Methods

Experiments involving animals were carried out in accordance with the guidelines established by the European Community Council Directive and approved by the National Council on Animal Care of the Italian Ministry of Health.

Animals

A mixed background line of mice (C57BL6:CD1) carrying a Scn1a gene ablation was used as in Yu et al. (2006) and Liautard et al. (2013). To disrupt the Scn1a gene, a replacement-type construct was targeted to the last coding exon (Yu et al. 2006; Liautard et al. 2013). Heterozygous mice and wild-type (WT) littermates (males or females) were selected for experiments. Age of mice was between postnatal day 16–18 (P16–P18), except for experiments displayed in Figure 4 that were performed on P15–P18 mice. To identify PV- and SST-positive interneurons, the mouse line Gt(ROSA)26Sortm14(CAG-tdTomato)Hze/J (here called simply "Tomato"), that carries the floxed Td-Tomato sequence under the ubiquitous promoter ROSA26, was crossed with the Pvalbtm1 (cre)Arbr/J (called "PV-Cre") mouse line, that expresses the Cre enzyme under the PV promoter or with the Ssttm 2.1(c re)Zjh/J (named "SST-Cre") that expresses the Cre enzyme under the somatostatin promoter, respectively. Double transgenic animals Gt(ROSA) 26Sortm14(CAG-tdTomato)Hze/J/Pvalbtm1(cre)A rbr/Ja (named "PV-Tomato") and Gt(ROSA)26Sortm14(CAG-tdTomato)Hze/J/Ssttm 2.1 (cre)Zjh /J ("SST-Tomato") were subsequently crossed with a Na$_V$-1.1-KO heterozygous mouse to achieve the triple transgenic mice, WT-PV-Tomato or Scn1a$^{-/+}$-PV-Tomato, and WT-SST-Tomato or Scn1a$^{-/+}$-SST-Tomato, respectively. Gt(ROSA)26Sortm14 (CAG-tdTomato)Hze/J (stock #007908), Pvalbtm1(cre)Arbr/J (stock #008069), and Ssttm 2.1(cre)Zjh /J (stock #13044) mouse lines were purchased from the Jackson Laboratory (Bar Harbor, ME, USA).

In Vivo Local Field Potential and Multiunit Activity Recording

Mice were anesthetized with 15% urethane (1.8 g/kg in physiological solution) and placed on a stereotaxic apparatus. The body temperature was constantly monitored and kept at 37 °C

with a heating blanket. To ensure a deep and constant level of anesthesia, vibrissae movement, eyelid reflex, response to tail, and toe pinching were visually controlled before and during the surgery. In some experiments, the oxygen saturation was controlled by a pulseoxymeter (MouseOx, Starr Life Sciences Corp., Oakmont, PA, USA), and respiration rate and heartbeat frequency were recorded. No significant difference was observed in the respiration rate and hearbeat frequency between WT and $Scn1a^{-/+}$ mice (respiration rate: 139 ± 4 vs. 129 ± 4 events/min in WT and $Scn1a^{-/+}$ mice, respectively, $P = 0.13$ unpaired Student's t-test; heartbeat frequency: 573 ± 8 vs. 555 ± 7 events/min, $P = 0.12$ unpaired Student's t-test, WT $N = 14$, $Scn1a^{-/+}$ $N = 13$). A local lidocaine injection was performed over the cranial area of interest and, after a few minutes, a longitudinal incision was performed to expose the skull. A small cranial window (<1 mm) was opened at coordinates (0 mm bregma, 3.5 mm lateral to sagittal sinus), roughly corresponding to the somatosensory area of the cortex, while keeping the surface of the brain moist with the normal HEPES-buffered artificial cerebrospinal fluid (aCSF). The dura was carefully removed using a metal needle. For awake head-restrained recordings, mice were anesthetized with ketamine/xylazine (Ketaset, 100 mg/mL/Rompun 20 mg/mL; 10 mL/g body weight). Surgery was performed as described for the anesthetized condition, with the only difference that small metal plaque was sealed on the mouse head to ensure better mechanical stability. Mice were kept at controlled body temperature until awakening.

To record local field potential (LFP) and multiunit activity (MUA) signals, bipolar custom-built tungsten electrodes (FHC, Inc., Bowdoin, ME, USA; distance between the tips ~300–350 μm, impedance 0.1 MΩ at 1 kHz) were inserted in the cortex. Electrical signals were acquired in the 0.1–5000 Hz band, amplified via an AM amplifier (AM System, Carlsborg, WA, USA) and digitized at 25–50 kHz using a Digidata 1440 interface and PClamp software (Molecular Device, Sunnyvale, CA, USA).

Slice Preparation and Patch-Clamp Recording

Animals were deeply anesthetized with urethane (1.8 g/kg) or Zoletil (40 mg/kg) and decapitated. The brain was quickly removed and immersed in the cold (4 °C) "cutting solution" containing (in mM): 125 NaCl, 2.5 KCl, 1.25 NaH$_2$PO$_4$, 25 NaHCO$_3$, 2 MgCl$_2$, 1 CaCl$_2$, 25 glucose, 2 Na-pyruvate, 3 Myo-inositol, and 0.4 ascorbic acid (pH 7.4, 95% O$_2$/5% CO$_2$). Coronal slices (300 μm thick) of neocortex were prepared with a vibratome (VT1000S, Leica Microsystems, GmbH, Wetzlar, Germany), incubated in cutting solution at 34 °C for 30 min, and then at room temperature for additional 30 min before transfer to the recording chamber. For experiments shown in Figure 4 after dissection, the brain was transferred to ice-cold standard aCSF (s-aCSF; in mM 125 NaCl, 2.5 KCl, 2 CaCl$_2$, 1 MgCl$_2$, 25 glucose, pH 7.4 with 95% O$_2$/5% CO$_2$). Slices (350 μm thick) were cut in the solution described in Dugue et al. (2005). Slices were then first transferred for 1 min in a 95% O$_2$/5% CO$_2$ saturated solution containing (in mM): 225 d-mannitol, 2.5 KCl, 1.25 NaH$_2$PO$_4$, 26 NaHCO$_3$, 25 glucose, 0.8 CaCl$_2$, 8 MgCl$_2$, 2 kynurenic acid with 95% O$_2$/5% CO$_2$, then transferred in s-aCSF at 30 °C for 20 min, and finally maintained at room temperature.

Recordings in Figures 3, 5C, 6C–8 were performed at 30–32 °C using an inline solution heater and a temperature controller (TC-344B, Warner Instruments, Hamden, CT, USA), while continuously perfusing the slices with aCSF bubbled with 95% O$_2$/5% CO$_2$ (pH 7.4). The aCSF contained (in mM): 125 NaCl, 2.5 KCl, 1.25 NaH$_2$PO$_4$, 25 NaHCO$_3$, 2 MgCl$_2$, 2 CaCl$_2$, and 25 glucose. For experiments in Figure 4, brain slices were continuously perfused at high rate with the following solution (in mM): NaCl, 120; KCl, 3.2;

KH$_2$PO$_4$, 1; NaHCO$_3$, 26; MgCl$_2$, 0.5; CaCl$_2$, 2; glucose, 10; at pH 7.4 (with 95% O$_2$/5% CO$_2$).

Patch-clamp, whole-cell recordings in Figures 3, 7, and 8 were performed in the infragranular layers of the neocortex of WT and $Scn1a^{-/+}$ mice. Pyramidal neurons were visually identified using infrared video microscopy and characterized by large somata and pia-oriented apical dendrites. PV- and SST-positive interneurons were identified using Tomato fluorescence in triple transgenic mice (see the previous section describing animals). To record spontaneous excitatory postsynaptic currents (sEPSCs, Fig. 7), glass electrodes (2.5–4 MΩ resistance) were filled with intracellular solution containing (in mM): 124 K-gluconate, 9 KCl, 10 HEPES, 1 EGTA, 2 MgCl$_2$, 4 MgATP, 0.3 Na$_3$GTP, pH adjusted to 7.2 with KOH, 280–300 mOsm. The estimated E_{Cl} was –60 mV based on the Nernst equation. sEPSCs were recorded at an holding potential of –60 mV and were blocked by D-(-)-2-amino-5-phosphono-pentanoic acid (D-APV, 50 μM) and 6,7-dinitroquinoxaline-2,3-dione disodium salt (DNQX, 10 μM). All drugs were purchased from Tocris Bioscience (Bristol, UK). To record spontaneous inhibitory postsynaptic currents (sIPSCs, Fig. 8) and autaptic activity, electrodes were filled with intracellular solution containing (in mM): 70 K-gluconate, 70 KCl, 10 HEPES, 1 EGTA, 2 MgCl$_2$, 4 MgATP, 0.3 Na$_3$GTP, pH adjusted to 7.2 with KOH, 280–300 mOsm. This solution generates an inhibitory GABAergic inward current, because the Nernst equation predicts an E_{Cl} about –16 mV and recordings were performed at the holding potential of –70 mV. D-APV (50 μM) and DNQX (10 μM) were added to the aCSF during experiments to block excitatory neurotransmission. All recorded IPSCs were blocked by the GABA$_A$ receptor antagonist gabazine (12.5 μM). Both intracellular solutions were used to record membrane excitability (Fig. 3). Access resistance was monitored throughout the recordings and was typically <20–25 MΩ. For experiments displayed in Figure 4, the intracellular pipette solution was (in mM): K-gluconate, 145; MgCl$_2$, 2; EGTA, 0.5; Na$_2$ATP, 2; Na$_3$GTP, 0.2; HEPES, 10; to pH 7.2 with KOH, osmolarity, 305–315 mOsm. For experiments displayed in Figures 5C and 6C, the intracellular pipette solution was (in mM): K-gluconate, 140; MgCl$_2$, 1; NaCl, 8; Na$_2$ATP, 2; Na$_3$GTP, 0.5; HEPES, 10; phosphocreatine, 10; to pH 7.2 with KOH, osmolarity, 295–310 mOsm. Data were not corrected for the liquid junction potential. Signals were amplified and filtered using a Multiclamp 700B patch-clamp amplifier (Molecular Device). Data were digitized at 50 kHz with a Digidata 1440 interface and pClamp software (Molecular Device).

Ictal Event Generation

Ictal event induction experiments were performed in the presence of 4-aminopyridine (4-AP; 50–100 μM) or in the presence of 0 Mg^{2+} containing extracellular solution. A pressure ejection unit (PDES, NPI Electronics, Tamm, Germany) was used to apply a single or double pulse to the NMDA (1 mM, Sigma Aldrich, Milano, Italy)-containing pipettes with a 3-s interval, a pressure of 4–10 psi, and a duration of 200–600 ms. The NMDA-containing pipette was positioned in vicinity of the rhinal fissure. The epileptogenic focus was defined as the region up to 300 μm from the pipette tip where neurons were directly activated by NMDA (Gomez-Gonzalo et al. 2010), while the ictal propagating region is the region distant at least 400 μm from the NMDA-containing pipette tip. All pyramidal neurons recorded were at a distance of 1 mm from the NMDA-containing pipette tip.

Virus Injection

Stereotaxic injection of AAVflex.CBA.Arch-GFP.WPRE.SV40 (Penn Vector Core, Philadelphia, PA, USA) was performed in the cortex

of PV-Cre and SST-Cre mice at P0 (P0 was considered as the day of birth). Pups were deeply anesthetized by hypothermia and immobilized on a customized stereotaxic apparatus. A small skin incision was performed along midline and viruses were injected with a glass micropipette in the somatosensory area of the cortex. Stereotaxic coordinates for injections were: 0 mm bregma, 1.5 mm lateral to sagittal sinus, and 0.25–0.3 mm depth. Approximately 200–300 nL of virus was slowly delivered into the brain for each animal. At the end the injection, the pipette was slowly withdrawn, the skin carefully sutured, and the pups quickly warmed and revitalized under a heating infrared lamp. Electrophysiological experiments were performed at 3–4 weeks after the injection.

Optogenetic Stimulation

Optical stimulation of Arch was achieved using a 594-nm solid-state laser source (Cobolt, Vretenvägen, Sweden). The laser was controlled by a command voltage, via an analog signal using an acousto-optic modulator (Gooch & Housego, USA). Light pulses were delivered to the brain through an optical fiber (200 μm diameter, AMS Technologies, Milan, Italy), which was located as close as possible to the surface of the brain slice (Figs 5C and 6C) or to the surface of the brain (Figs 5D,E and 6D,E). For combined electrophysiological and optogenetic experiments in vivo, the fiber was placed parallel to the recording bipolar electrode to minimize optical artifacts (Cardin et al. 2010). To gradually modulate the effect of the optogenetic perturbation on the firing properties of interneurons, light intensity was titrated through the use of neutral density filters (placed in the optical path between the laser source and the fiber optic) and ranged between approximately 3 and 30 mW (measured at the fiber tip). Light pulse duration was 500 ms in all experiments displayed in Figures 5 and 6.

Two-Photon Targeted Juxtasomal Recording

A laser scanning Ultima scanhead (Bruker Italia, Milan, Italy) coupled with an Ultra II Cameleon laser source (Coherent Italy, Milan, Italy) was used to monitor Tomato fluorescence using 720 nm light wavelength. Animal preparation was performed as described previously but without removing the dura. Electrophysiological juxtasomal recordings were performed with borosilicate glass pipettes (2 mm outer diameter, 3–7 MΩ resistance in brain tissue), which were filled with extracellular solution containing (in mM): NaCl 127, KCl 3.2, CaCl$_2$ 2, MgCl$_2$ 1, HEPES 10, and Alexa Fluor 488, pH 7.4. Pipettes were initially lowered through the pia applying a positive pressure (250 mbar) until the depth of interest (150–300 μm) was reached. At this point, a lower positive pressure (25 mbar) was applied. Based on the fluorescence image of Tomato-positive cells and of Alexa Fluor 488, the pipette was slowly moved towards the target cell. When a contact between the pipette and the fluorescent cell was achieved, the positive pressure was released and a dim negative pressure was applied to facilitate the formation of the juxtasomal recording configuration (resistance 40–400 MΩ). Electrical signals were amplified by an ELC-01X amplifier (NPI Electronics), digitized by an ITC-18 interface (InstruTECH Corporation, Port Washington, NY, USA), and acquired using Patchmaster (HEKA Elektronik, Lambrecht, Germany).

Immunohistochemistry and Confocal Image Acquisition

Under deep urethane anesthesia, animals were transcardially perfused using 0.01 M PBS pH 7.4, followed by 4% paraformaldehyde (PFA) in PBS. Brains were subsequently removed, post-fixed for 6 h in PFA, incubated in a 30% sucrose PBS solution for cryoprotection, and finally cut with a cryostat (Leica Microsystems Italia, Milan, Italy) in coronal slices of 40 μm thickness. Floating slices from fluorescent tissue (Fig. 2) were collected, mounted on glass slides using Vectashield (Vector Laboratories, Peterborough, UK) or [1,4-diazobicyclo-(2,2,2)octane] (DABCO)-based antifade mounting medium, and coverslipped. For immunofluorescence staining (Figs 2, 5A,B, and 6A,B), floating sections were incubated for at least 24 h at 4 °C in primary antibody diluted in 5% NGS in 0.3% Triton-X 100 in PBS. After washing in PBS, the slices were incubated in 0.3% Triton-X 100 in PBS for 2 h at room temperature in the appropriate secondary antibody. Some sections were then stained with Hoechst for 30 min at room temperature, and mounted on glass slides using DABCO-based antifade mounting medium. Primary antibodies used were: anti-GABA (1 : 1000, rabbit, Sigma A2052); anti-somatostatin (1 : 100, rat, Millipore MAB354); and anti-PV (1 : 1000, mouse, Sigma P3088). Secondary antibodies used were: Alexa 488 (1 : 800, goat anti-rabbit, Invitrogen A11034); Alexa 647 (1 : 800, goat anti-rabbit, Invitrogen A21245); and Alexa 647 (1 : 800 goat anti-mouse, Invitrogen A21236).

Data Analysis

Analysis of LFP and MUA signals was performed using customized Matlab code (Matlab, Natick, MA, USA). For LFP analysis, extracellular potentials were down-sampled (1 kHz) and low-pass filtered (cutoff frequency, 100 Hz). A power spectrum was generated for each recorded animal using a hamming window (window length: 4096 points, 50% overlap) on recording traces of approximately 5–10 min duration. Power spectra were normalized to the total signal power in the 0.1–100 Hz interval. In the normalized spectra, power values corresponding to different frequency bands (0.5–1 Hz, slow oscillations; 2–4 Hz, delta oscillations; 4–8 Hz, theta oscillations; 8–14 Hz, alpha spindles; 30–90 Hz, gamma oscillations) were calculated for both WT and Scn1a$^{-/+}$ mice. For MUA analysis, extracellular signals were high-pass filtered (cutoff frequency, 300 Hz) and thresholded according to a value set 5 times the standard deviation of the baseline signal (baseline). The baseline was chosen as a time window of >0.5 s where no extracellular spikes occurred. Spontaneous down- to up-state transitions were identified as the time point in which the signal crossed the threshold. Up- to down-state transitions were identified as the time points in which the MUA signal crossed the threshold and remained below the threshold for longer than 100 ms. Up- and down-state durations were calculated from the time of the down-to-up and the up-to-down transitions. Up-states shorter than 10 ms were not considered true up-states. Spikes were identified using a first-derivative spike-sorting algorithm.

In Figure 4, the recruitment of principal neurons into propagating ictal events was marked by the transition from the predominant inhibitory to the predominant excitatory phase (t$_{IE}$), which was defined as the timing in which the ratio between the inhibition and the excitation index was for the first time <0.1. Inhibition and excitation indices were calculated, respectively, as the part of the positive and the negative components of the time derivative of the trace which exceeded 5 times the mean standard deviation evaluated during the baseline (Cammarota et al. 2013). Ictal event duration in voltage-clamp recordings was calculated from the t$_{IE}$ to the end of the last afterdischarge recorded with an instant frequency higher than 0.1 Hz.

For the optogenetic experiments (Figs 5D,E and 6D,E), 3 temporal windows were considered: 100 ms before the light stimulation, 500 ms during the laser stimulus, and 100 ms after the light

illumination. At least 6 sweeps for each experiment were analyzed. The spectral content of the LFP signal was quantified by calculating the short-time Fourier transform over a moving Hamming window of 100 ms. Power values were normalized to the total power in the "pre" period.

For experiments in Figures 9 and 10, to obtain the spike train, we first applied a high-pass filter to the mean-subtracted juxtasomal signal (Kaiser filter with zero phase-lag and 0.5 Hz bandwidth, small passband ripple, 0.05 dB, and high stopband attenuation, 60 dB, cutoff frequency, 100 Hz). We then used a detection threshold. Depending on the noise level, the threshold varied across cells resulting in a mean value for PV-positive and SST-positive cells of 7.3 and 9.4 times the standard deviation of the filtered juxtasomal signal, respectively. The interspike interval (ISI, Figs 9D and 10D) was defined as the time interval between 2 consecutive action potentials (APs), while the coefficient of variations of the ISI (CV_{ISI}) was defined as the ratio of the standard deviation to the mean of the ISI distribution.

In brain slice experiments, the average frequency of APs (Fig. 3B,D,F) was calculated for increasing depolarizing current injections (50 pA step, 600 ms duration). The input resistance (R_{in}, Table 5) was calculated from hyperpolarizing current injections; AP threshold was measured at the inflection point of rising phase of the AP; AP amplitude was measured between the threshold and the AP peak; AP duration was measured at half height between threshold and peak; the AP rise time was calculated as the difference between the time of occurrence of the AP threshold and the time of the AP maximum positive peak. Autaptic currents were elicited in the voltage-clamp configuration by a short voltage depolarization (from a holding potential of −70 to 0 mV, 0.3–1.0 ms duration) as in Bacci and Huguenard (2006). Autaptic currents were blocked by application of gabazine (12.5 μM) and their amplitude was measured at the peak. In combined electrophysiological and optogenetic experiments (Figs 5C and 6C), the frequency of APs was calculated in a time window of 350 ms before and after the light stimulus and in a time window of 500 ms during light stimulation. Detection of sEPSCs and sIPSCs was performed with Minianalysis (Synaptosoft, Inc., Fort Lee, NJ, USA) using a threshold criterion, setting the threshold at 3 times the standard deviation of the baseline noise. Detected events were visually inspected and artifactual events removed. The median of the distribution of amplitudes and interevent intervals (IEIs) for both sEPSCs and sIPSCs was calculated for each recorded cell. Mean values provided in the result section were calculated by averaging the medians across cells. Offline analysis was carried out with Clampfit 10.2, application of pClamp 10.2 (Molecular Device), MiniAnalysis (Synaptosoft, Decatur, GA, USA), and Origin 8.6 (OriginLab Corporation, Northampton, MA, USA).

Statistics

Values are expressed as mean ± SEM. To evaluate normality, a Kolmogorov–Smirnov normality test was run on each experimental sample. When comparing 2 populations of data, Student's t-test was used to calculate statistical significance in case of Gaussian distribution; otherwise, the nonparametric Mann–Whitney test was used. This choice reflects the standard practice in statistics (Box et al. 2005) to use the parametric test (that has more statistical power) whenever the appropriate conditions are applicable, and to use a more general, but less statistically sensitive, test when the conditions for applying the parametric test are not met. When multiple populations of data were compared, one- or two-way ANOVA with Bonferroni post hoc tests were used in case of Gaussian distribution. The

nonparametric Friedman with Dunn post hoc test was used in Figures 5D and 6C,D. The Kolmogorov–Smirnov test for experiments in Figures 9C,E and 10B,D. All tests were two-sided.

Results

Cortical Network Activities in WT and $Scn1a^{-/+}$ Mice In Vivo

We performed extracellular LFP and MUA recordings in the deep regions (~700 μm) of the neocortex of urethane-anesthetized WT and heterozygous $Scn1a^{-/+}$ mice during the pre-epileptic period (P16–P18, Fig. 1). Under this type of anesthesia, neocortical circuits are spontaneously active (Crunelli and Hughes 2010). A main component of these intrinsic activities is the slow oscillation (Metherate et al. 1992; Steriade, Contreras, et al. 1993; Steriade et al. 1993a, 1993b). This rhythm is observed both at the level of individual cells (Steriade et al. 1993b; Petersen, Hahn, et al. 2003) and mass signals (Steriade, Contreras, et al. 1993). During the slow oscillation, neurons alternate between an up-state, characterized by elevated firing, and a down-state, characterized by neuronal silence (Steriade, Contreras, et al. 1993; Steriade 2006). As expected, spontaneous network activity in WT and heterozygous $Scn1a^{-/+}$ mice was dominated by this rhythmic activity (Fig. 1B). LFP recordings were quantified by calculating the signal power in different frequency bands (see Materials and Methods) and comparison between WT and $Scn1a^{-/+}$ mice was performed (Fig. 1C). $Scn1a^{-/+}$ mice displayed no significant change in the power of slow (frequency interval: 0.5–1 Hz), delta (2–4 Hz), theta (4–8 Hz), alpha spindles (8–14 Hz), and gamma (30–90 Hz) oscillations compared with the WT controls (Table 1). We further quantified spontaneous network dynamics by analyzing the MUA signal, which mainly reflected the suprathreshold activity of neurons (Logothetis 2003), and we found no significant differences in spike activity between the 2 genotypes. Average values of up-state parameters were: up-state frequency, 0.91 ± 0.08 versus 0.93 ± 0.06 Hz ($P = 0.8$, unpaired Student's t-test) for WT and $Scn1a^{-/+}$ mice; average up-state duration, 0.29 ± 0.04 versus 0.23 ± 0.02 s ($P = 0.18$, unpaired Student's t-test) for WT and $Scn1a^{-/+}$ mice; average down-state duration: 1.09 ± 0.26 versus 0.97 ± 0.12 s ($P = 0.90$, Mann–Whitney test) for WT and $Scn1a^{-/+}$ mice; average number of spikes per up-state: 45 ± 9 versus 31 ± 6 ($P = 0.30$, Mann–Whitney test) for WT and $Scn1a^{-/+}$ mice. WT, $N = 17$; $Scn1a^{-/+}$, $N = 19$.

Given the heterogeneity in cortical circuits across different tissue depth (Adesnik and Scanziani 2010; Feldmeyer 2012; Beltramo et al. 2013), we asked whether disrupting the $Scn1a$ gene could have different effects on deep versus more superficial cortical regions. To tackle this question, we repeated the extracellular recordings described previously at approximately 300 μm depth. Besides a small, but significant, decrease in the average power of oscillations in the delta (2–4 Hz) and theta (4–8 Hz) frequency band, the LFP signal was largely unaffected in superficial cortical areas in $Scn1a^{-/+}$ mice compared with controls (Table 2), as observed in deeper regions (Fig. 1B,C). Analysis of the MUA signal in recordings performed at approximately 300 μm depth confirmed unaltered up-state frequency, up-state duration, down-state duration, and number of spikes per up-state in $Scn1a^{-/+}$ compared with WT mice. Average up-state frequency: 0.74 ± 0.07 versus 0.62 ± 0.05 Hz ($P = 0.13$, Mann–Whitney test) for WT and $Scn1a^{-/+}$ mice; average values of up-state duration: 0.22 ± 0.03 versus 0.20 ± 0.01 s ($P = 0.95$, Mann–Whitney test); average values of down-state duration: 1.48 ± 0.30 versus 1.60 ± 0.15 s ($P = 0.08$, Mann–Whitney test); average number of spikes per up-
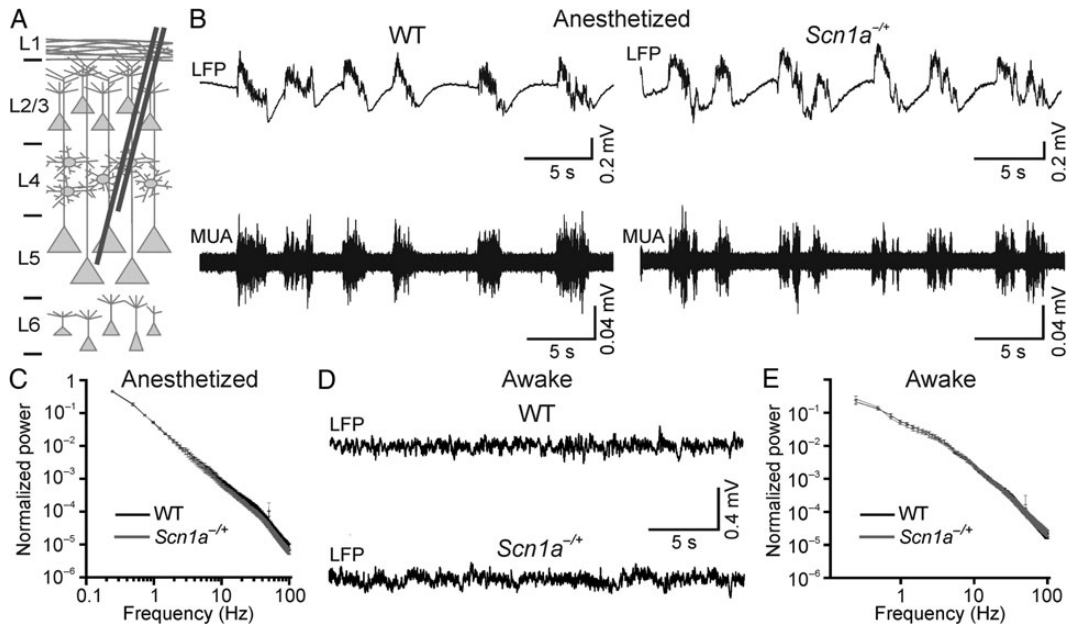
Figure 1. Cortical network dynamics in WT and *Scn1a*$^{-/+}$ mice in vivo. (A) Schematic representation of experimental configuration. Recording electrodes were placed at approximately 700 μm depth. (B) Representative traces of LFP (top traces) and MUA (bottom traces) activity in anesthetized WT (left) and *Scn1a*$^{-/+}$ (right) mice during spontaneous activity. (C) Average normalized LFP power spectra for WT ($N = 18$) and *Scn1a*$^{-/+}$ mice ($N = 17$). (D) Representative traces of LFP in awake head-restrained WT (top) and *Scn1a*$^{-/+}$ (bottom) mice showing spontaneous activity. (E) Average normalized LFP power spectra in awake, head-restrained mice. WT, $N = 15$; *Scn1a*$^{-/+}$ mice, $N = 15$.

Table 1 Average LFP power values in deep cortical regions of anesthetized mice

Frequency band (Hz)	WT average normalized power values (a.u), $N = 18$ animals	*Scn1a*$^{-/+}$ average normalized power values (a.u), $N = 17$ animals
0.5–1	0.36 ± 0.02	0.36 ± 0.02
2–4	0.08 ± 0.01	0.07 ± 0.01
4–8	0.035 ± 0.005	0.027 ± 0.003
8–14	0.019 ± 0.003	0.014 ± 0.002
30–90	0.011 ± 0.002	0.008 ± 0.001

Note: Statistical significance was evaluated with the Mann–Whitney test.

Table 2 Average LFP power values in superficial cortical areas of anesthetized mice

Frequency band (Hz)	WT average normalized power values (a.u), $N = 18$ animals	*Scn1a*$^{-/+}$ average normalized power values (a.u), $N = 16$ animals
0.5–1	0.30 ± 0.02	0.33 ± 0.02
2–4	0.11 ± 0.01	0.08 ± 0.01**
4–8	0.06 ± 0.01	0.04 ± 0.01*
8–14	0.05 ± 0.01	0.04 ± 0.01
30–90	0.029 ± 0.004	0.020 ± 0.004

Note: Statistical significance was evaluated with the Mann–Whitney test.
*$P < 0.05$; **$P < 0.01$.

state: 25 ± 6 versus 21 ± 3 ($P = 0.99$, Mann–Whitney test). WT, $N = 17$; *Scn1a*$^{-/+}$, $N = 18$.

Since urethane has diffuse effects on both inhibitory and excitatory neurotransmission (Petersen, Grinvald, et al. 2003; Dombeck et al. 2007), anesthesia could potentially mask the effect of disrupting the *Scn1a* gene by inducing abnormal circuits dynamics. To address this concern, we repeated the experiments displayed in Figure 1B,C in awake, head-restrained mice placing

Table 3 Average LFP power values in deep cortical areas in awake mice

Frequency band (Hz)	WT average normalized power values (a.u), $N = 15$ animals	*Scn1a*$^{-/+}$ average normalized power values (a.u), $N = 15$ animals
2–4	0.19 ± 0.02	0.17 ± 0.01
4–8	0.095 ± 0.008	0.097 ± 0.007
8–14	0.052 ± 0.004	0.052 ± 0.005
30–90	0.027 ± 0.004	0.023 ± 0.001

Note: Statistical significance was evaluated with the unpaired Student's *t*-test.

the metal electrodes initially in deep cortical regions (~700 μm). As shown in Figure 1D,E, under these experimental conditions, network activities were different from those observed under urethane anesthesia (Fig. 1B,C). The LFP was dominated by small amplitude, high-frequency oscillations that were in contrast with the large amplitude, low-frequency oscillations observed in the anesthetized condition. However, similar to the anesthetized condition, no significant differences were detected in the LFP signal in *Scn1a*$^{-/+}$ mice compared with controls (Table 3). The lower frequency band (0.5–1 Hz) was excluded in this analysis because of the larger movement artifacts in the awake compared with the anesthetized animal preparation, which mainly affected the lower frequency band (<1 Hz). Recordings in more superficial cortical regions (~300 μm depth) confirmed no significant difference in the signal power in any frequency band that was analyzed in *Scn1a*$^{-/+}$ mice compared with controls (Table 4).

Decreased Excitability of Specific Classes of Interneurons in Brain Slices From *Scn1a*$^{-/+}$ Mice

Previous studies pointed to the dysfunction in interneuronal excitability as the main cellular alteration leading to SMEI (Yu et al. 2006; Ogiwara et al. 2007; Cheah et al. 2012; Han et al. 2012). Given that interneuronal firing tightly controls the output of principal

Table 4 Average LFP power values in superficial cortical areas in awake mice

Frequency band (Hz)	WT average normalized power values (a.u), $N = 15$ animals	$Scn1a^{-/+}$ average normalized power values (a.u), $N = 15$ animals
2–4	0.15 ± 0.02	0.14 ± 0.02
4–8	0.08 ± 0.01	0.08 ± 0.01
8–14	0.06 ± 0.01	0.06 ± 0.01
30–90	0.027 ± 0.004	0.028 ± 0.005

Note: Statistical significance was evaluated with unpaired Student's *t*-test.

cells (Freund and Katona 2007; Cardin et al. 2009; Sohal et al. 2009; Isaacson and Scanziani 2011), it is somewhat surprising to observe no difference in spontaneous network activities in $Scn1a^{-/+}$ mice in vivo (Fig. 1). We thus decided to directly measure the excitability of interneurons in our experimental model, focusing on 2 main subpopulations: PV- and SST-expressing cells, which account for approximately 70% of the total interneuronal population in the cortex (Rudy et al. 2011). To identify PV- and SST-positive interneurons in WT and $Scn1a^{-/+}$ mice, we generated triple transgenic animals expressing the red fluorescent protein Td-Tomato (Tomato) specifically in these cellular subtypes (Fig. 2). Floxed Tomato mice were crossed either with the
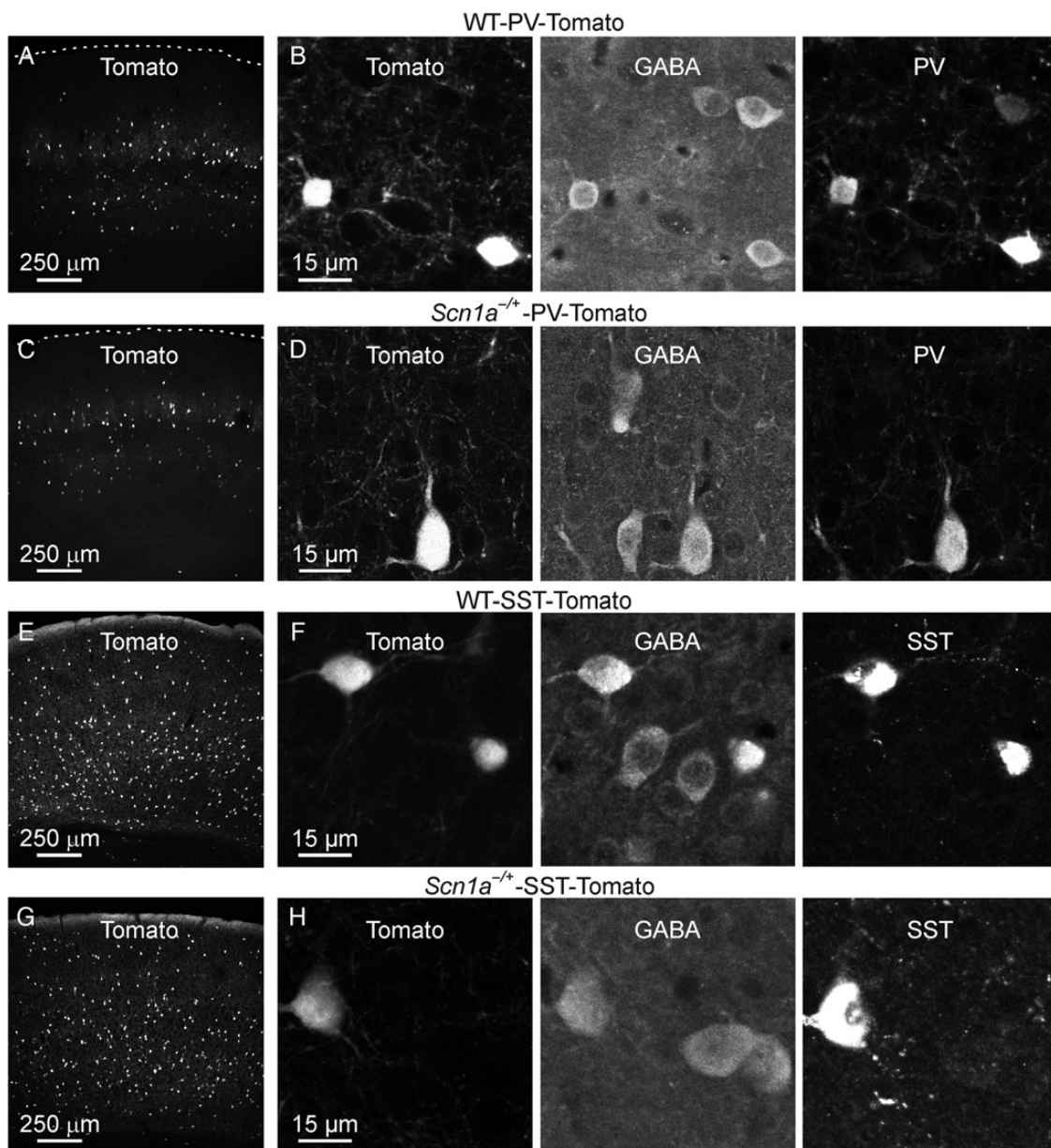
Figure 2. Identification of genetically specified subclasses of interneurons in WT and $Scn1a^{-/+}$ mice. (*A*) Confocal image showing Tomato fluorescence in a section from the cortex of a WT-PV-Tomato mouse. (*B*) A zoom in of 2 Tomato-positive cells is shown in the leftmost panel. The section shown in (*B*) was stained against GABA (middle panel) and PV (rightmost panel). (*C* and *D*) Same as in *A* and *B* for $Scn1a^{-/+}$-PV-Tomato. (*E* and *F*) Same as in *A* and *B* for WT-SST-Tomato. (*G* and *H*) Same as in *A* and *B* for $Scn1a^{-/+}$-SST-Tomato.

PV-Cre mouse line that expressed the Cre enzyme under the PV promoter or with the SST-Cre line that expressed the Cre enzyme under the SST promoter. Heterozygous double transgenic animals were then crossed with $Scn1a^{-/+}$ mice to achieve WT-PV-Tomato (Fig. 2A,B) or $Scn1a^{-/+}$-PV-Tomato (Fig. 2C,D) and WT-SST-Tomato (Fig. 2E,F) or $Scn1a^{-/+}$-SST-Tomato (Fig. 2G,H) mice, respectively. These animals were then used for patch-clamp experiments in slices (Fig. 3) from the somatosensory cortex at P16–P18 (the same cortical region and the same time interval used for in vivo recordings). We first performed recordings from pyramidal neurons that were visually identified with differential interference contrast. All recorded cells had a regular firing discharge pattern (Fig. 3A) and a main apical dendrite, which was visible under the microscope, all features that are typical of pyramidal cortical neurons (Contreras 2004). In current-clamp configuration, we recorded the membrane potential response to hyperpolarizing and depolarizing current injections. The average frequency of APs discharged at a given current injection was similar between WT and $Scn1a^{-/+}$ mice (Fig. 3B, interaction, $P > 0.99$, two-way repeated-measures ANOVA with Bonferroni post hoc test, $N = 27$ cells for both WT and $Scn1a^{-/+}$), as were the biophysical properties of recorded neurons (Table 5). We then recorded from Tomato-positive neurons in WT-PV-Tomato and $Scn1a^{-/+}$-PV-Tomato transgenic mice (Fig. 3C). In WT-PV-Tomato (simply called WT in Fig. 3C,D), fluorescent cells displayed the typical features of fast-spiking PV-positive interneurons (Ascoli et al. 2008; DeFelipe et al. 2013), including high frequency of AP firing, small adaptation, and low input resistance (Fig. 3C and Table 5). However, in $Scn1a^{-/+}$-PV-Tomato mice (simply called $Scn1a^{-/+}$ in Fig. 3C,D), the discharge pattern of fluorescent cells was deeply affected compared with WT controls. Cells displayed a delayed or stuttering fast-spiking behavior, which resulted in a decreased average frequency of AP firing upon current injections (Fig. 3C,D, interaction, $P < 1E - 5$, two-way repeated-measures ANOVA with Bonferroni post hoc test, $N = 21$ and 28 cells for WT and $Scn1a^{-/+}$, respectively). We finally performed recordings from Tomato-positive neurons in WT-SST-Tomato transgenic mice. We found that fluorescent cells displayed substantial adaptation in their AP firing, higher input resistance, and longer spikes compared with fluorescent cells in PV-Tomato animals (Fig. 3E and Table 5), all features that are typical of SST cells. In $Scn1a^{-/+}$-SST-Tomato mice, fluorescent cells had similar electrophysiological properties, although the average frequency of APs discharged upon current injection was significantly decreased for higher values of current injections in cells from these mice compared with controls (Fig. 3E,F, interaction, $P < 1E - 5$, two-way repeated-measures ANOVA with Bonferroni post hoc test, $N = 25$ and 28 cells for WT and $Scn1a^{-/+}$, respectively).
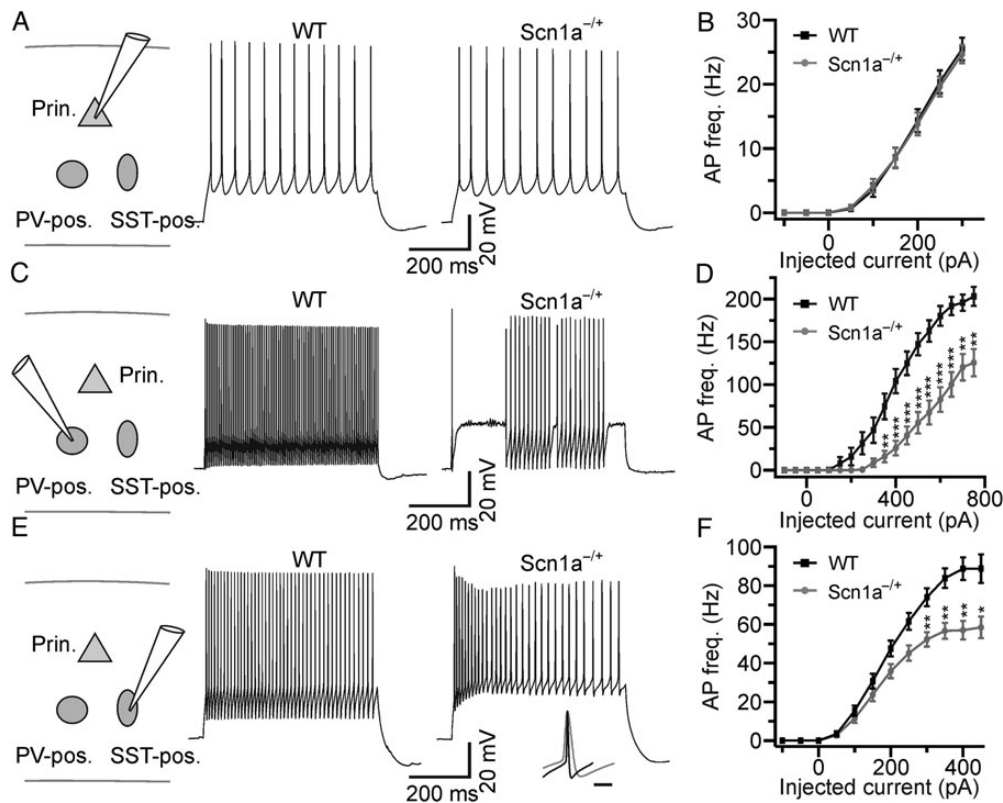
Figure 3. Cell type-specific dysfunction of excitability in brain slices from $Scn1a^{-/+}$ mice. (A) Left: schematic of the experimental configuration. Prin., principal neuron; PV-pos., parvalbumin-positive interneuron; SST-pos., somatostatin-positive interneuron. Right: representative current-clamp recordings from pyramidal neurons recorded from WT (left) and $Scn1a^{-/+}$ (right) mice in cortical slice. (B) Average frequency of AP firing in principal neurons as a function of injected current for WT ($N = 27$ cells, black) and $Scn1a^{-/+}$ ($N = 27$ cells, gray). (C) Representative current-clamp recordings from Tomato-positive interneurons recorded in cortical slices from a WT-PV-Tomato (WT, left) and a $Scn1a^{-/+}$-PV-Tomato ($Scn1a^{-/+}$, right) mouse. (D) Average frequency of AP firing as a function of injected current for fluorescent cells recorded in WT-PV-Tomato mice ($N = 21$, black) and $Scn1a^{-/+}$-PV-Tomato mice ($N = 28$, gray). The asterisks indicate significance at each value of current injection evaluated with the Bonferroni post hoc test. In this as well as in other figures: *$P < 0.05$; **$P < 0.01$; ***$P < 0.001$. (E) Representative current-clamp recordings from Tomato-positive cells recorded in cortical slices from WT-SST-Tomato (left) and $Scn1a^{-/+}$-SST-Tomato (right) animals. The inset shows the overlap of one AP recorded in a PV-positive cell from a $Scn1a^{-/+}$-PV-Tomato mouse and one AP recorded in a SST-positive cell from a $Scn1a^{-/+}$-SST-Tomato mouse. Traces are normalized to the AP maximal amplitude. Scale bar 10 ms. (F) Average frequency of AP firing as a function of injected current for cells recorded in WT-SST-Tomato animals ($N = 25$, black) and $Scn1a^{-/+}$-SST-Tomato animals ($N = 28$, gray).

Table 5 Biophysical properties of recorded neurons

	Principal cells		PV-positive cells		SST-positive cells	
	WT (N = 27 cells)	$Scn1a^{-/+}$ (N = 27 cells)	WT (N = 21 cells)	$Scn1a^{-/+}$ (N = 28 cells)	WT (N = 25 cells)	$Scn1a^{-/+}$ (N = 28 cells)
R_{in} (MΩ)	103 ± 9	107 ± 9	109 ± 8	86 ± 5*	208 ± 16	195 ± 14
AP amplitude (mV)	84 ± 2	85 ± 1	66 ± 2	63 ± 2	72 ± 2	71 ± 2
AP duration (ms)	1.04 ± 0.05	1.09 ± 0.04	0.36 ± 0.01	0.39 ± 0.01	0.65 ± 0.02	0.79 ± 0.04**
AP rise time (ms)	0.59 ± 0.03	0.59 ± 0.02	0.37 ± 0.01	0.40 ± 0.01*	0.56 ± 0.02	0.63 ± 0.02**
AP threshold (mV)	−42.6 ± 0.7	−42.0 ± 0.8	−41.7 ± 1.1	−42.4 ± 0.9	−42.1 ± 0.8	−42.5 ± 0.7

Note: Statistical significance was evaluated with unpaired Student's t-test. $^*P < 0.05$; $^{**}P < 0.01$.
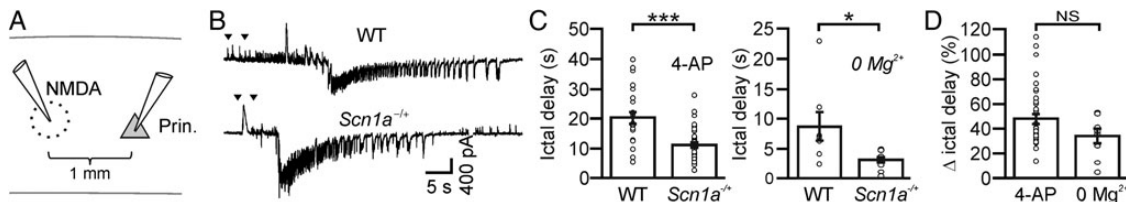
Figure 4. Faster propagation of focal ictal discharges in slices from $Scn1a^{-/+}$ mice. (A) Schematic of the experimental configuration for the generation of focal ictal discharges. (B) Representative voltage-clamp recordings at −50 mV of an NMDA-induced ictal event in a pyramidal neuron 1 mm away from the NMDA application site in a WT (top) and a $Scn1a^{-/+}$ (bottom) mouse. (C) Left: average delays of ictal onset in pyramidal neurons from WT (N = 24 ictal events from 11 mice) and $Scn1a^{-/+}$ (N = 38 ictal events from 12 mice) animals in the presence of 4-AP. Right: average delays of ictal onset in pyramidal neurons from WT (N = 8 ictal events from 2 mice) and $Scn1a^{-/+}$ (N = 9 ictal events from 2 mice) animals in low Mg^{2+} (0 Mg^{2+}). (D) Average values of ictal onset delay normalized to control in 4-AP (N = 38 ictal events from 12 mice) and low Mg^{2+} (N = 9 ictal events from 2 mice).

Faster Propagation of Focal Ictal Discharges in Slices From $Scn1a^{-/+}$ Mice

The decrease in interneuronal firing of inhibitory cells observed in $Scn1a^{-/+}$ mice may alter the propensity to generate epileptiform activity. To test this possibility, we probed cortical networks of WT and $Scn1a^{-/+}$ mice with local applications of NMDA (Fig. 4) that resulted in generation and propagation of focal seizure-like, ictal discharges (Gomez-Gonzalo et al. 2010; Losi et al. 2010). NMDA was initially applied in the presence of the proconvulsant 4-AP (Gomez-Gonzalo et al. 2010; Losi et al. 2010). By using patch-clamp recordings from pyramidal neurons, we monitored the ictal discharge propagation at 1 mm from the focal area (the NMDA application site). We found that, in slices from $Scn1a^{-/+}$ mice, local NMDA applications evoked in pyramidal neurons long-lasting ictal events characterized by the typical tonic/clonic transition phase that had a similar duration as the ictal events evoked in cortical slices from WT mice (Fig. 4A, average ictal duration, 78 ± 8 vs. 74 ± 10 s; N = 38 events from 12 $Scn1a^{-/+}$ mice and N = 24 events from 11 WT mice; P = 0.73, unpaired Student's t-test). However, ictal events recorded in $Scn1a^{-/+}$ mice occurred after the NMDA pulse application with a delay significantly shorter than in WT mice (Fig. 4C, left histogram, P = 2.7E − 5, Mann–Whitney test and Fig. 4D). We repeated similar experiments in a different model of ictal generation, in which we applied the NMDA pulses while perfusing the slice with a nominally Mg^{2+}-free extracellular solution (0 Mg^{2+}). Also under these experimental conditions, the onset of the ictal event in the pyramidal neurons distant from the focus occurred with a shorter delay in $Scn1a^{-/+}$ mice with respect to WT controls (Fig. 4C, right histogram, P = 0.023, unpaired Student's t-test). Consistent with this shorter delay, the number of the pre-ictal inhibitory barrages, which are evoked in pyramidal neurons mainly by PV-expressing fast-spiking interneurons (Cammarota et al. 2013), was reduced in $Scn1a^{-/+}$ with respect to WT mice (5 ± 1 vs. 11 ± 1, N = 17 ictal

events from 4 $Scn1a^{-/+}$ mice and N = 17 ictal events from 5 WT mice; P = 2.5E − 3, unpaired Student's t-test).

Acute Inhibition of PV- and SST-Positive Interneurons Modifies Ongoing Network Dynamics

In vivo experiments in both anesthetized and awake animals showed no major changes in spontaneous network activities in $Scn1a^{-/+}$ mice (Fig. 1). These in vivo results seem difficult to interpret in light of the significant cell-specific dysfunction observed in slice recordings (Fig. 3). One possibility is that a reduction in the excitability of PV- and SST-interneurons in vivo does not significantly alter spontaneous, nonepileptic network dynamics. To test this hypothesis directly, we acutely decreased the firing activities of PV- and SST-positive interneurons in vivo using inhibitory optogenetic manipulations and light titration (see Materials and Methods). We expressed the inhibitory opsin Archaerhodopsin (Arch) specifically in PV- or SST-positive interneurons by injecting adeno-associated viruses carrying a double-floxed Arch sequence in PV-Cre (Fig. 5) or SST-Cre (Fig. 6) WT animals, respectively. Immunohistological analysis confirmed that the majority of opsin-positive cells stained for GABA both in PV-Cre (Fig. 5B) and in SST-Cre (Fig. 6B) animals. Moreover, using intracellular patch-clamp recordings in brain slices, we confirmed that illumination with yellow light (λ = 594 nm) significantly reduced AP firing in both PV-Cre (Fig. 5C, P = 0.022, one-way repeated-measures ANOVA test with Bonferroni post hoc test) and SST-Cre (Fig. 6C, P = 2.3E − 5, Friedman test with Dunn's post hoc test)-injected animals.

We then investigated the effect of acutely reducing AP firing in PV- and SST-positive cells on spontaneous network dynamics by combining extracellular recordings with optogenetic photoinhibition in awake, head-restrained mice. We delivered pulses of yellow light (stimulus duration of 500 ms) to the cortical surface
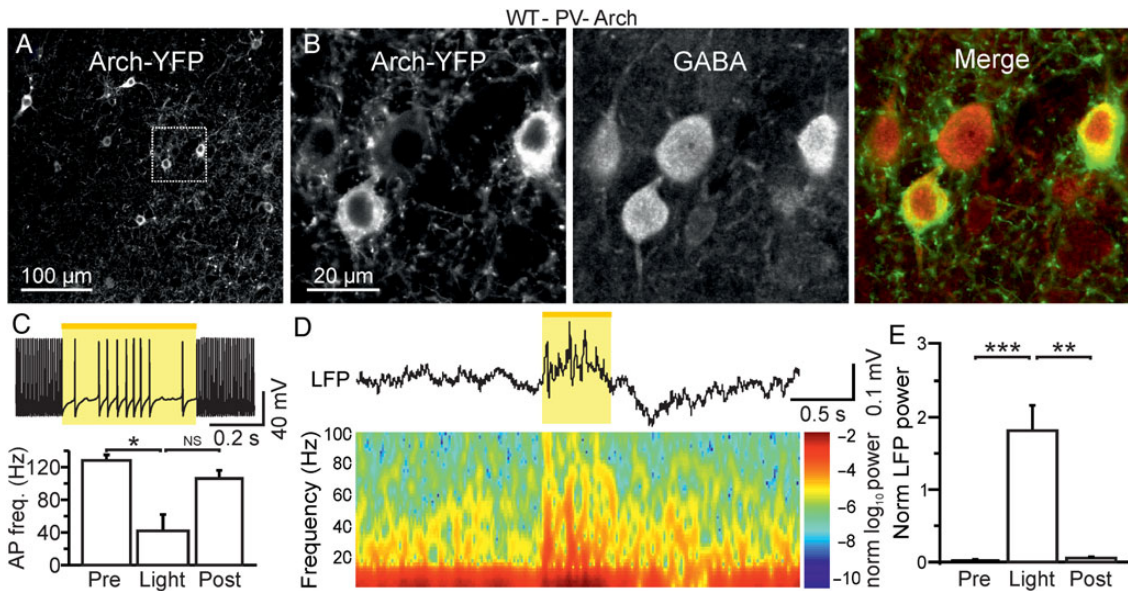
Figure 5. Acute optogenetic reduction of firing in PV-positive cells affects ongoing network dynamics in vivo. (A) Confocal image of a cortical section from a WT-PV-Cre animal which was injected with AAV-transducing Arch-YFP. (B) A zoom in of 2 Arch-YFP-positive cells (leftmost panel) is shown. The same section shown in (B) was stained for GABA (middle panel). The merge of the 2 images is shown in the rightmost panel. (C) Top: slice recording displaying a membrane potential response to yellow light pulse in a representative Arch-positive neuron. AP discharge was elicited in the recorded neuron by current injection (600 pA). Bottom: Histogram displaying the average AP frequency before (pre), during (stim), and after (post) light stimulation in $N = 4$ recorded cells. (D) Representative LFP trace (top) and corresponding spectrogram (bottom) showing the effect of yellow light illumination on spontaneous cortical activity in awake, head-restrained WT-PV-Cre animals which were injected with AAVs carrying a double-floxed Arch sequence. (E) Average values of normalized LFP power before (pre), during (stim), and after (post) light stimulation ($N = 11$ mice). LFP power was calculated in the spectral range of 30–90 Hz.
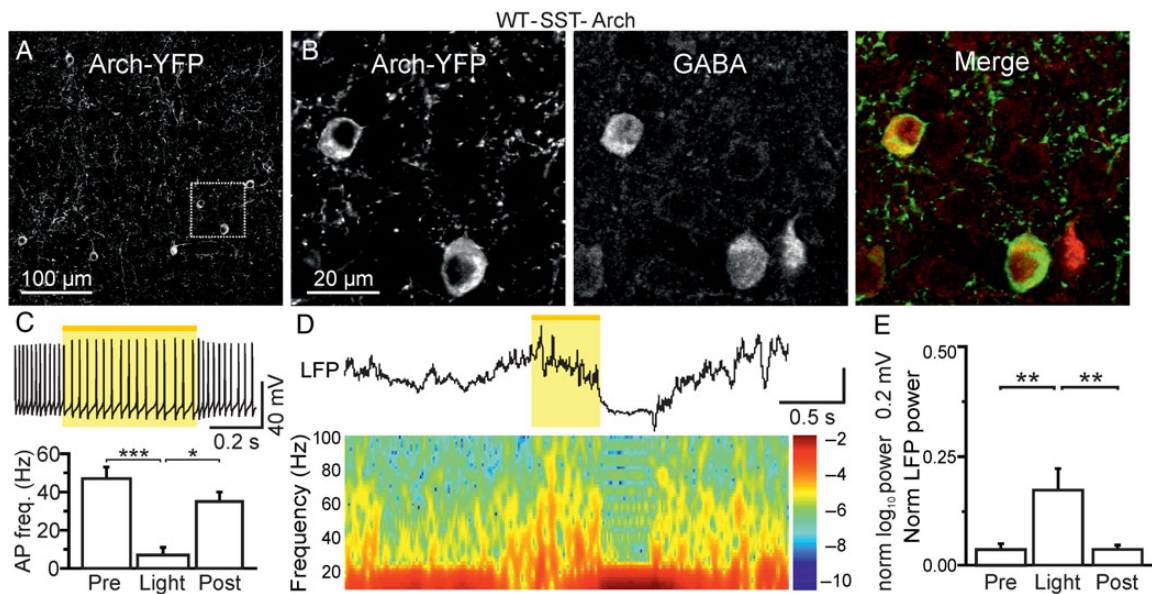

Figure 6. Acute optogenetic reduction of firing in SST-positive cells affects ongoing network dynamics in vivo. (A) Confocal image of a cortical section from a WT-SST-Cre animal which was injected with AAV-transducing Arch-YFP. (B) A zoom in of 2 Arch-YFP-positive cells (leftmost panel) is shown. The same section shown in (B) was stained for GABA (middle panel). The merge of the 2 images is shown in the rightmost panel. (C) Top: slice recording displaying membrane potential response to yellow light pulse in a representative Arch-positive neuron. AP discharge was elicited in the recorded neuron by current injection (300 pA). Bottom: Histogram displaying the average AP frequency before (pre), during (stim), and after (post) light stimulation in $N = 12$ recorded cells. (D) Representative LFP trace (top) and corresponding spectrogram (bottom) showing the effect of yellow light illumination on spontaneous cortical activity in awake, head-restrained WT-SST-Cre animals which were injected with AAVs carrying a double-floxed Arch sequence. (E) Average values of normalized LFP power before (pre), during (stim), and after (post) light stimulation ($N = 9$ mice). LFP power was calculated in the spectral range of 30–90 Hz.

through an optical fiber. In injected PV-Cre and SST-Cre animals, yellow light illumination reliably affected ongoing cortical activities. In all injected PV-Cre mice ($N = 11$), light illumination led to

alterations in the LFP that started after light onset and ended at light cessation (Fig. 5D, top). The power of most LFP frequencies increased as shown in the corresponding spectrogram (Fig. 5D,

bottom), especially in the gamma band (Fig. 5E, $P < 1E - 4$, Friedman test with Dunn's Multiple Comparison test). In animals expressing Arch in SST-positive interneurons, yellow light illumination also caused a change in the ongoing circuit activities recorded with the LFP. High-frequency oscillations were significantly increased upon yellow light illumination (Fig. 6D,E, $P = 3E - 4$, Friedman test with Dunn's Multiple Comparison test). At the end of the light stimulation, a period of low oscillatory activity was observed (Fig. 6D). This latter finding is compatible with the rebound firing activity that characterizes a subpopulation of SST-positive cells following membrane hyperpolarization (Ascoli et al. 2008; DeFelipe et al. 2013).

Synaptic Changes in $Scn1a^{-/+}$ Mice

Optogenetic experiments described previously (Figs 5 and 6) demonstrate that acute silencing of PV- or SST-positive interneurons significantly affected spontaneous network dynamics, suggesting that, besides reduced excitability of interneurons, additional mechanisms may come into play and account for the unaltered network activity observed in vivo (Fig. 1). One possibility is that interneuronal dysfunction is counterbalanced by changes in synaptic properties. To address this hypothesis, we investigated excitatory and inhibitory synaptic currents in cortical slices from WT and $Scn1a^{-/+}$ animals. We first recorded sEPSCs from pyramidal (Fig. 7A,B), PV-positive (Fig. 7C,D), and SST-positive (Fig. 7E,F) cells. We found that the amplitude of sEPSCs was significantly increased in pyramidal cells (Fig. 7B, left panel; average amplitude: 10.7 ± 0.6 vs. 8.2 ± 0.4 pA for $N = 10$ cells in $Scn1a^{-/+}$ mice and $N = 7$ cells in WT mice, respectively, $P = 9.9E - 3$, unpaired Student's t-test), while sEPSC amplitude

was unchanged in PV-positive cells (Fig. 7D, left panel; average amplitude: 18.5 ± 0.7 vs. 16.2 ± 1.1 pA, $P = 0.10$, unpaired Student's t-test, $N = 7$ cells for both $Scn1a^{-/+}$ and WT) and SST-positive interneurons (Fig. 7F, left panel; average amplitude: 13.8 ± 3.2 vs. 12.2 ± 1.7 pA, $P = 0.94$, Mann–Whitney test, $N = 6$ cells for both $Scn1a^{-/+}$ and WT). The IEI of sEPSCs was not significantly different in pyramidal cells (Fig. 7B, right panel; average IEI: 0.14 ± 0.04 vs. 0.19 ± 0.04 s in $N = 10$ cells in $Scn1a^{-/+}$ mice and $N = 7$ cells in WT mice, respectively, $P = 0.11$, Mann–Whitney test), PV-positive cells (Fig. 7D, right panel; average IEI: 0.050 ± 0.010 vs. 0.029 ± 0.003 s, $P = 0.08$, unpaired Student's t-test, $N = 7$ cells for both $Scn1a^{-/+}$ and WT), and SST-positive cells (Fig. 7F, right panel; average IEI: 0.17 ± 0.02 vs. 0.17 ± 0.05 s, $P = 0.98$, unpaired Student's t-test, $N = 6$ cells for both $Scn1a^{-/+}$ and WT). We then recorded sIPSCs (Fig. 8) and found that their amplitude was significantly increased in PV-positive cells (Fig. 8D, left panel; average amplitude: 34.5 ± 4.6 vs. 21.0 ± 2.5 pA for $N = 8$ cells in $Scn1a^{-/+}$ mice and $N = 8$ cells in WT animals, respectively, $P = 0.02$, unpaired Student's t-test), while it was unchanged in pyramidal neurons (Fig. 8B, left panel; average amplitude: 17.5 ± 1.8 vs. 17.6 ± 1.6 pA, $P = 0.97$, unpaired Student's t-test, $N = 8$ cells for both $Scn1a^{-/+}$ and WT) and SST-positive cells (Fig. 8F, left panel; average amplitude: 15.6 ± 1.1 vs. 13.6 ± 1.2 pA, $P = 0.24$, unpaired Student's t-test, $N = 8$ cells for both $Scn1a^{-/+}$ and WT). The IEI of sIPSCs was unaffected in pyramidal neurons (Fig. 8B, right panel; average IEI: 0.17 ± 0.04 vs. 0.17 ± 0.03 s for $N = 8$ cells in $Scn1a^{-/+}$ mice and $N = 8$ cells in WT animals, respectively, $P = 0.96$, unpaired Student's t-test), PV-positive cells (Fig. 8D, right panel; average IEI: 0.15 ± 0.03 vs. 0.16 ± 0.04 s, $P = 0.88$, unpaired Student's t-test, $N = 8$ cells for both $Scn1a^{-/+}$ and WT), and SST-positive cells (Fig. 8F, right panel; average IEI: 0.38 ± 0.06 vs. 0.38 ± 0.06 s, $P = 0.95$, unpaired
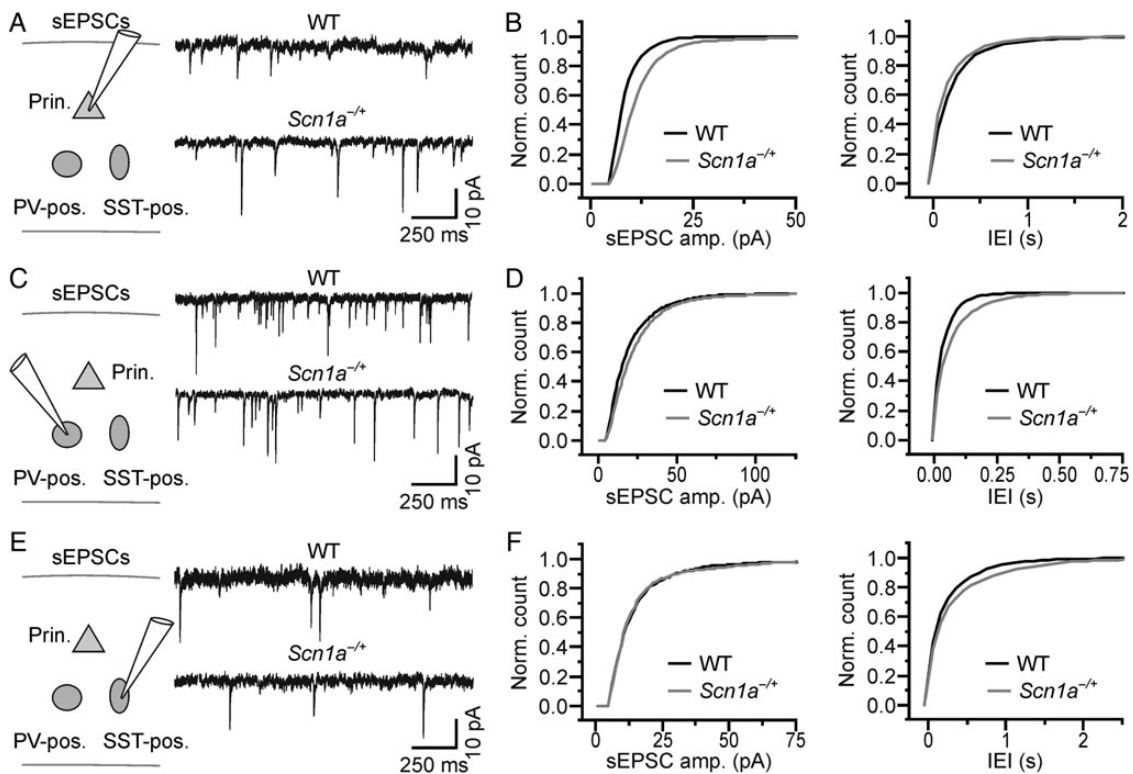

Figure 7. Cell type-specific changes in sEPSCs in brain slices from $Scn1a^{-/+}$ mice. (A) Left: schematic of the experimental configuration. Recordings were performed from principal cortical neurons. Right: sEPSCs in slices from WT (top) and $Scn1a^{-/+}$ (bottom) animals recorded from principal neurons. (B) Cumulative distribution of the amplitude (left) and frequency (right) of sEPSCs recorded from WT ($N = 7$ cells) and $Scn1a^{-/+}$ ($N = 10$ cells). (C,D and E,F) same as in (A and B) for sEPSCs recorded from PV-positive (WT, $N = 7$ cells; $Scn1a^{-/+}$, $N = 7$ cells) and SST-positive (WT, $N = 6$ cells; $Scn1a^{-/+}$, $N = 6$ cells) interneurons, respectively.
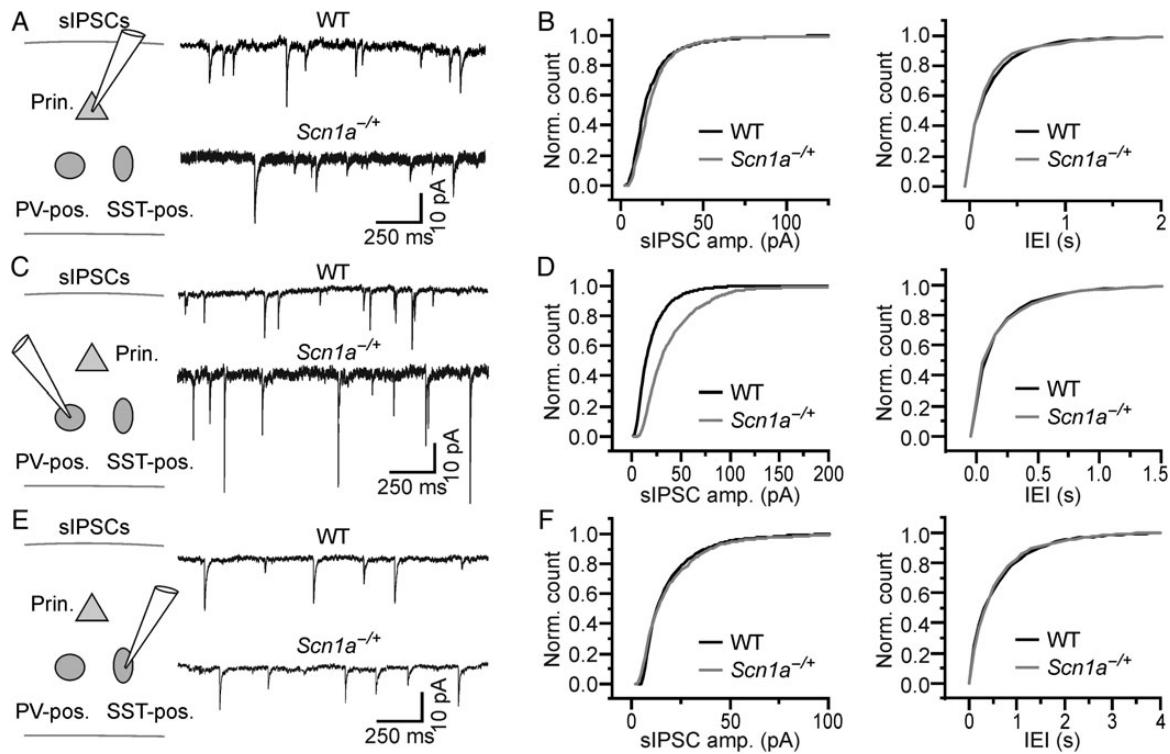
Figure 8. Cell type-specific changes in sIPSCs in brain slices from *Scn1a*$^{-/+}$ mice. (A) Left: schematic of the experimental configuration. Recordings were performed from principal cortical neurons. Right: sIPSCs in slices from WT (top) and *Scn1a*$^{-/+}$ (bottom) animals recorded from principal neurons. (B) Cumulative distribution of the amplitude (left) and frequency (right) of sIPSCs recorded from WT (*N* = 8 cells) and *Scn1a*$^{-/+}$ (*N* = 8 cells). (C,D) and (E,F) same as in (A and B) for sIPSCs recorded from PV-positive (WT, *N* = 8 cells; *Scn1a*$^{-/+}$, *N* = 8 cells) and SST-positive (WT, *N* = 8 cells; *Scn1a*$^{-/+}$, *N* = 8 cells) interneurons, respectively.

Student's *t*-test, *N* = 8 cells for both *Scn1a*$^{-/+}$ and WT). Moreover, the amplitude of GABAergic autaptic currents onto PV-positive interneurons was also significantly increased in slices from *Scn1a*$^{-/+}$ mice compared with controls (data not shown; average amplitude of autaptic GABAergic current: 475 ± 99 vs. 211 ± 97 pA, *P* = 0.02, Mann–Whitney test, *N* = 15 for *Scn1a*$^{-/+}$ mice and *N* = 14 for WT, respectively).

Spontaneous Firing Activities of Individual Interneurons In Vivo

The decreased firing rate in interneurons upon somatic current injections that we observed in slices from *Scn1a*$^{-/+}$ mice (Fig. 3) is larger for higher values of current injections, especially in SST-positive interneurons (Fig. 3F). It is important to understand whether these changes in interneuronal excitability are also detected in the intact brain, where cells are driven to fire by physiological synaptic currents. To this aim, we recorded the firing of individual, genetically identified interneurons in vivo during spontaneous network activities. We first targeted PV-positive neurons. We performed two-photon-guided juxtasomal recordings in anesthetized WT-PV-Tomato (simply called WT in Fig. 9) and *Scn1a*$^{-/+}$-PV-Tomato (called *Scn1a*$^{-/+}$). Using two-photon microscopy, we visualized individual Tomato-positive cells and recorded their firing activity in juxtasomal configuration (Fig. 9B). Figure 9C displays the distributions of average firing rates in all the recorded cells in WT (left) and *Scn1a*$^{-/+}$ (right) mice, which were not significantly different (*P* = 0.16, *N* = 15 WT and *N* = 14 *Scn1a*$^{-/+}$ animals, Kolmogorov–Smirnov test). The average distributions of ISIs (Fig. 9D, interaction ISI bin-transgene *P* = 0.16, *N* = 32 WT and *N* = 34 *Scn1a*$^{-/+}$ animals, two-way repeated-measures ANOVA) and the distributions of the CV$_{ISI}$

(Fig. 9E, *P* = 0.15, *N* = 15 WT and *N* = 14 *Scn1a*$^{-/+}$ animals, Kolmogorov–Smirnov test) were also not significantly different between WT and *Scn1a*$^{-/+}$.

We then recorded from SST-positive interneurons (Fig. 10). The distributions of average firing rates in all the recorded cells in WT and *Scn1a*$^{-/+}$ mice were not significantly different (Fig. 10B, *P* = 0.97, *N* = 12 WT and *N* = 11 *Scn1a*$^{-/+}$ animals, Kolmogorov–Smirnov test). The average ISI distributions (Fig. 10C, interaction ISI bin-transgene *P* = 0.96, *N* = 27 WT and *N* = 21 *Scn1a*$^{-/+}$ animals, two-way repeated-measures ANOVA) and the distributions of CV$_{ISI}$ (Fig. 10D, *P* = 0.22, *N* = 12 WT and *N* = 11 *Scn1a*$^{-/+}$ animals, Kolmogorov–Smirnov test) were also unaffected in *Scn1a*$^{-/+}$ compared with WT controls, confirming no major changes in interneuronal firing during spontaneous activity in vivo.

Discussion

Identifying early dysfunctions of neuronal networks before the onset of the symptoms of SMEI is fundamental to develop a therapeutic approach of this intractable disease. Here, we have investigated the activity of cortical microcircuits at the network and cellular level during the pre-epileptic period in *Scn1a*$^{-/+}$ mice, a widespread experimental model of SMEI. To our knowledge this is the first analysis of single-cell firing during in vivo network activity in a mouse model of SMEI.

Unaltered Spontaneous Network Dynamics in *Scn1a*$^{-/+}$ Mice In Vivo

In our in vivo experiments, we found that spontaneous cortical dynamics over a large frequency range, including gamma oscillations, were largely similar in *Scn1a*$^{-/+}$ mice compared with WT
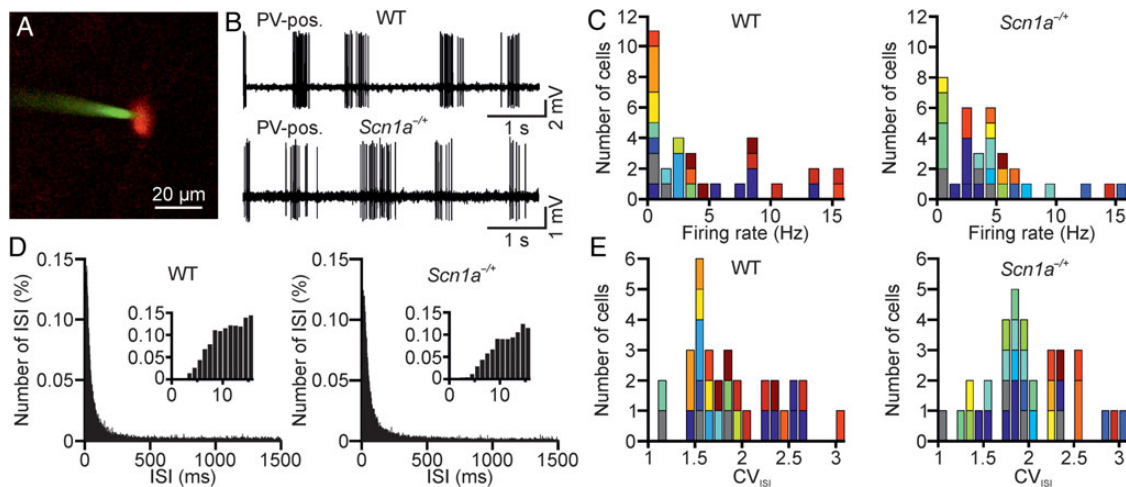
Figure 9. Two-photon-guided juxtasomal recordings from PV-positive interneurons in vivo. (A) Two-photon image showing a Tomato-positive (red signal) layer II interneuron in an anesthetized WT-PV-Cre mouse which was crossed with a Tomato reporter mouse line. Under visual control, a glass pipette filled with Alexa 488 (green signal) is lowered within the cortical tissue until a juxtasomal recording is obtained with a genetically identified cell. (B) Juxtasomal recording from a Tomato-positive cell in a WT (top) and $Scn1a^{-/+}$ (bottom) mouse. (C) Distribution of the average firing rate of recorded cells in WT (left, $N = 32$ cells from 15 different animals) and $Scn1a^{-/+}$ (right, $N = 34$ cells from 14 different animals). Cells recorded from the same animal are displayed with the same color code. (D) Average (over cells) distribution of the ISI in WT (left) and $Scn1a^{-/+}$ (right) for the same set of recordings analyzed in C. Bin, 1 ms. The distributions are shown at an expanded time scale in the insets. (E) Distribution of the CV_{ISI} in WT (left) and $Scn1a^{-/+}$ (right). Same color code as in C.
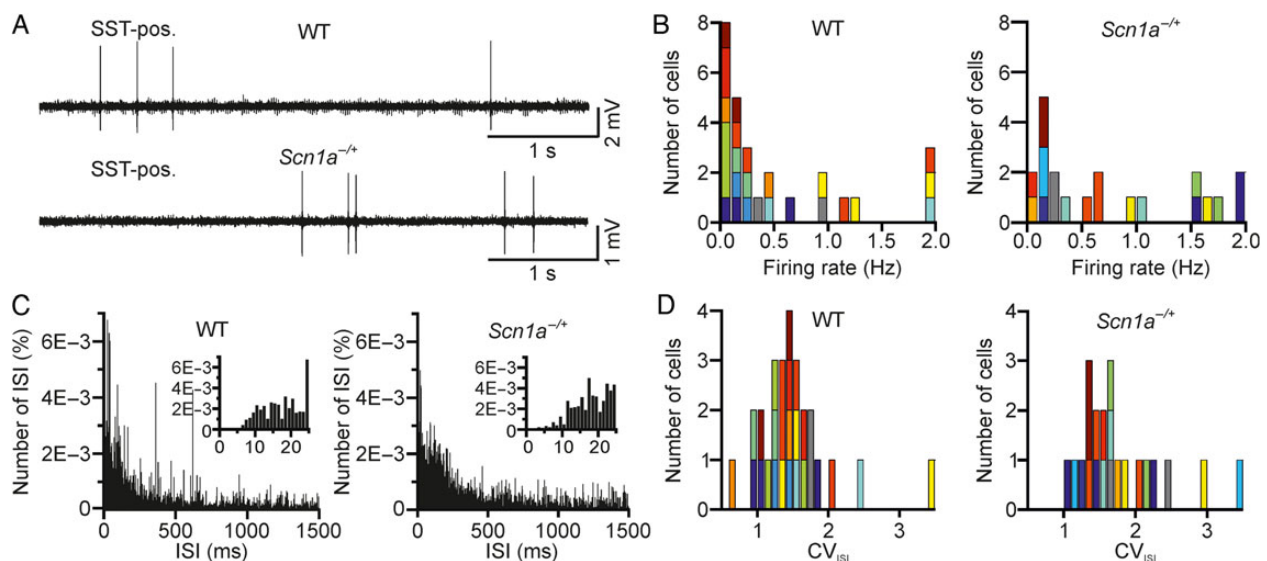

Figure 10. Two-photon-guided juxtasomal recordings from SST-positive interneurons in vivo. (A) Juxtasomal recording from a Tomato- and SST-positive cell in anesthetized WT (top) and $Scn1a^{-/+}$ (bottom) mice. (B) Distribution of the average firing rate of recorded cells in WT (left, $N = 27$ cells from 12 different animals) and $Scn1a^{-/+}$ (right, $N = 21$ cells from 11 different animals). The color code indicates cells recorded in different animals. (C) Average (over cells) distribution of the ISI in WT (left) and $Scn1a^{-/+}$ (right) for the same set of recordings analyzed in B. Bin, 1 ms. The distributions are shown at an expanded time scale in the insets. (D) Distribution of the CV_{ISI} in WT (left) and $Scn1a^{-/+}$ (right). Same color code as in C.

controls (Fig. 1). Most importantly, this finding was independent from the depth of the cortical recording (see Results) and it was confirmed in both anesthetized (Fig. 1B,C) and awake, head-restrained (Fig. 1D,E) mice. These results suggest that no major alterations in local network activities are observed throughout the neocortex during the pre-epileptic period in $Scn1a^{-/+}$ animals. This surprising finding is at odds with previously published data reporting strongly decreased excitability of interneurons in $Scn1a^{-/+}$ mice (Yu et al. 2006; Ogiwara et al. 2007; Cheah et al. 2012; Han et al. 2012; Tai et al. 2014). Indeed, these interneuronal deficits were proposed to be the major pathophysiological mechanism of SMEI. Moreover, the markedly altered firing of inhibitory

interneurons was expected to produce other prominent global cortical effects, given the crucial role of inhibitory circuits in controlling cortical network dynamics (Isaacson and Scanziani 2011), including oscillations in the beta-gamma frequency band (Cardin et al. 2009; Sohal et al. 2009; Uhlhaas and Singer 2010; Hu et al. 2014).

Interneuronal Hypoexcitability and Synaptic Changes in Cortical Slices From $Scn1a^{-/+}$ Mice

To correctly interpret our results in light of previous work, we directly measured cellular firing properties in slice preparation in

our experimental model (Fig. 3). We have examined 3 key elements of the cortical circuitry: The excitatory principal neurons and 2 major classes of inhibitory cells, perisomatic-targeting PV-positive basket cells and dendrite-targeting SST-expressing interneurons. We found that the biophysical properties and the excitability of principal neurons were not significantly affected (Fig. 3A,B), while a decreased efficacy in AP generation upon depolarizing current injections was observed in PV-positive (Fig. 3C,D) and SST-positive (Fig. 3E,F) neurons. Although hypoexcitability was observed in both PV- and SST-positive interneurons, PV-positive cells displayed a pronounced reduction in firing over a wide range of current injections. In contrast, SST-positive cells displayed reduced excitability only for larger values of current injection. These data are in large agreement with previous reports demonstrating that, in acutely isolated cells and brain slices, the excitability of interneurons, but not that of pyramidal cells, is decreased in $Scn1a^{-/+}$ mice (Yu et al. 2006; Ogiwara et al. 2007; Cheah et al. 2012; Han et al. 2012). These results also confirm that, in brain slices, interneuronal dysfunction is observed in different classes of inhibitory cells (PV- and SST-positive; Tai et al. 2014).

In brain slices, we further investigated the effect of the $Scn1a$ gene deletion on synaptic currents. We recorded sEPSCs and sIPSCs, respectively, in principal cells (Figs 7A,B and 8A,B), PV-positive (Figs 7C,D and 8C,D), and SST-positive (Figs 7E,F and 8E, F) interneurons. The largest effects that we observed were an increase in the amplitude of sEPCS in principal cells (Fig. 7B, left panel) and an increase in the amplitude of sIPSCs in PV-positive cells (Fig. 8D, left panel). Interestingly, a prominent source of inhibition of PV-positive cells, autaptic self-inhibition (Bacci and Huguenard 2006; Deleuze et al. 2014), was also significantly increased in $Scn1a^{-/+}$ mice (see the Results section). We did not observe changes in the IEI of sEPSCs and sIPSCs under our experimental conditions (Figs 7B,D,F and 8B,D,F), in contrast to what previously reported in this (Yu et al. 2006; Ogiwara et al. 2007; Cheah et al. 2012; Han et al. 2012) and other models of Na$_V$1.1 channelopathies (Gu et al. 2014; Hedrich et al. 2014; Tsai et al. 2015). Differences in the recorded cell type, brain area, and animal age could account for these discrepancies. Taken together, our results suggest that altered functionality of Nav$_{1.1}$ channels leads to homeostatic synaptic changes, which affect the excitatory and inhibitory synaptic weight differently in distinct elements of the cortical microcircuit. Overall, the most prominent effect is a stronger synaptic inhibition of interneurons, especially PV-positive cells. If exacerbated during development, this specific alteration of inhibition on PV-positive cells could lead to a disinhibitory mechanism that could favor the outbreak of epileptic seizures during the onset of the disease. In support of this view, epileptiform events were found to propagate faster in slices from $Scn1a^{-/+}$ mice compared with controls (Fig. 4).

It is known that alterations of neuronal excitability lead to the homeostatic scaling of synaptic strength (Turrigiano and Nelson 2004). However, the mechanisms underlying synaptic scaling during homeostatic plasticity are still poorly understood. In $Scn1a^{-/+}$ mice, changes in neuronal excitability are restricted to inhibitory interneurons, possibly leading to the scaling of specific synapses, and therefore further complicating the interpretation at the network level. For example, increased inhibitory strength onto PV cells could be triggered by a homeostatic upscaling of GABAergic synapses in a cell-autonomous manner. Increased inhibitory strength on PV cells may result in disinhibition of pyramidal neurons, which might then open a window of opportunity for pyramidal neurons to partially escape a prominent inhibitory control and therefore increase the strength of their

glutamatergic synapses, possibly through a postsynaptic mechanism (Turrigiano and Nelson 2004). However, since the gene deletion does not affect PV cells only, the differential involvement of different interneuron subtypes, and their specific role within the cortical circuit, makes it very difficult to provide a clear mechanistic picture at a more global level. It will be therefore fundamental to reveal the specific synaptic mechanisms underlying the homeostatic control of cortical networks during the pre-epileptic period in $Scn1a^{-/+}$ mice and how this control falls apart during the onset of the severe seizure activity characterizing this devastating disease.

Extrapolating In Vivo Cellular and Network Dynamics From Slice Experiments

Slice recordings point to interneuronal dysfunction and potential circuit disinhibition as the main alterations occurring in the pre-epileptic period in the cortex of $Scn1a^{-/+}$ mice (Figs 3, 7, and 8). Based on these findings, major changes would be expected at the network level in the intact brain. In contrast, our in vivo recordings (Fig. 1) demonstrated unaltered spontaneous network dynamics in both anesthetized and awake mice. How to reconcile these apparent conflicting results? Can we directly compare in vitro with in vivo results? In other words, how far can we extrapolate in vitro results to the in vivo condition? First, it is important to remind that the firing activity of cortical cells in vivo is largely triggered by incoming synaptic inputs and not by artificial current injections. These inputs are driven by ongoing circuit activities (Petersen, Hahn, et al. 2003; Harris and Mrsic-Flogel 2013; Sachidhanandam et al. 2013) that involve and are sustained by the activity of a huge number of cells and much larger number of synaptic connections. For example, recurrent spontaneous activities observed in the cortex during anesthesia (the so-called slow oscillations) are observed in virtually all cortical neurons (Steriade, Contreras, et al. 1993; Steriade et al. 1993a, 1993b), spread as traveling waves over millimeters of cortical tissue (Massimini et al. 2004), and are strongly influenced by synaptically connected areas, such as the contralateral cortex (Mohajerani et al. 2010) or the thalamus (David et al. 2013; Sheroziya and Timofeev 2014). Second, in brain slices, many of these local and long-range synaptic connections are inevitably severed, thus preventing the recurrent excitatory drive (Crunelli and Hughes 2010) and potentially fundamental neuromodulatory effects (Marder 2012; Carracedo et al. 2013) that can deeply influence cellular spiking activity and network dynamics. Third, intracellular recordings in brain slices sample the activity of a limited number of cells and synaptic connections, numbers that are orders of magnitude smaller than the thousands of cells and synapses involved in the regulation of in vivo circuit dynamics. This massive undersampling, together with the aforementioned limitations of the in vitro preparation, suggests that it might not always be straightforward to precisely predict the outcome of a given genetic manipulation on network function in vivo based exclusively on slice recordings.

Unaltered Interneuronal Firing During Spontaneous Cortical Dynamics in $Scn1a^{-/+}$ Mice In Vivo

In the attempt to explain our contrasting in vitro and in vivo results, we directly measured interneuronal firing activity in vivo during spontaneous network dynamics. Surprisingly, we found that both PV- and SST-positive interneurons displayed a similar firing rate, interspike time interval, and coefficient of variation in $Scn1a^{-/+}$ mice with respect to controls (Figs 9 and 10). These

findings agree with the unaltered network dynamics that we observed in vivo with LFP and MUA recordings (Fig. 1), but contrast with the marked reduction in excitability that we observed in brain slices (Fig. 3C–F). Various mechanisms may explain these different results. For example, PV- and SST-positive cells in $Scn1a^{-/+}$ mice fire less spikes in response to prolonged depolarizing current injections (Fig. 3), and this effect is stronger at stimuli that elicit high-frequency firing in control mice, especially for SST-positive interneurons (Fig. 3F). This suggests that in $Scn1a^{-/+}$ mice, interneurons may behave normally, at frequencies below a certain threshold, but they might lose their ability to fire at higher frequency, for example, during epileptic discharges. Indeed, previous reports indicated that fast-spiking cortical interneurons in vivo can fire at up to 800 Hz during seizure activity (Timofeev et al. 2002), and this could play a role in controlling seizure propagation (Cammarota et al. 2013). It is therefore possible that during the spontaneous activity in the asymptomatic pre-epileptic period, interneurons are not forced to fire at those high frequencies and thus no phenotype is visible at the network level. If the network is challenged with a strong stimulus (e.g., a local NMDA application), network abnormalities become visible. Experiments in Figure 4 are in line with this hypothesis. However, it should also be noted that in our recordings of spontaneous activity, PV- and SST-positive interneurons in vivo fire with an instantaneous frequency up to 160 and 80 Hz (Figs 9D and 10C). At these rates, significant dysfunctions are already observed in brain slice experiments (Fig. 3D,F). Nevertheless, few APs are discharged with high instantaneous frequencies across cells: 10–15% in PV-positive cells with instantaneous frequency >50 Hz (Fig. 9D, inset) and 1–3% in SST-positive cells with instantaneous frequency with >50 Hz (Fig. 10C, inset).

An alternative possibility is that compensatory mechanisms may mask the dysfunction of GABAergic cell excitability observed in slices from $Scn1a^{-/+}$ mice. For example, homeostatic changes at the synaptic (Turrigiano and Nelson 2004) or circuit (Marder 2011) level may counteract interneuronal hypofunction and result in unaltered network activity. Synaptic alterations are indeed observed in $Scn1a^{-/+}$ mice (Liautard et al. 2013; Tai et al. 2014) both at the level of inhibitory and excitatory synapses (Figs 7 and 8). However, the mechanisms underlying the cell type-specific changes of excitatory and inhibitory synaptic transmission in $Scn1a^{-/+}$ mice described here remain to be elucidated. As described above, the most prominent effects are stronger synaptic excitation of principal neurons (Fig. 7B, left panel) and stronger synaptic inhibition of PV-positive interneurons (Fig. 8D, left panel), which would, however, predict increased network hyperexcitability and disinhibition rather than compensation. In any case, for the reasons explained previously, it is difficult to predict the impact of these changes on network activities in vivo. In this regard, it is interesting to note that acute optogenetic reduction of AP firing in both PV- and SST-positive interneurons in awake WT mice affected ongoing network activities. These data demonstrate that acute reduction of the excitability in both interneuronal subtypes elicits significant network effects, suggesting that interneuronal dysfunction may not be the only alteration present during the pre-epileptic period in $Scn1a^{-/+}$ mice and that potential additional cellular mechanisms may come into play. For example, homeostatic rearrangements may counteract the effect of the mutation in the pre-epileptic period, but might not be sufficient to block the development of seizures in the epileptic period. This is consistent with the resistance of induction of ictal activity with application of 4-AP in the pre-epileptic period (Yu et al. 2006; Liautard et al. 2013).

Since $Na_V1.1$ channels are expressed for quite a long distance along the axon initial segment (Ogiwara et al. 2007), it is possible that decreased conduction fidelity between the soma and the axon terminal may occur in $Scn1a^{-/+}$ mice, particularly at high firing rates. In transgenic mice in vivo, axonal conduction failure may thus occur independently of somatic action potentials. Moreover, $Na_V1.1$ channels may be expressed in cortical interneurons other than PV- and SST-positive cells, and these other interneuron subtypes may play an important role in the pathogenesis of SMEI. Finally, another possibility is that the abnormalities in membrane excitability observed in the slice experiments become apparent only under certain stressful conditions such as hyperthermia-induced alkalosis (Schuchmann et al. 2006, 2011). Future experiments will be crucial to test these hypotheses.

In summary, in this study, we investigated the cellular and network abnormalities arising in the pre-epileptic period in a mouse model of SMEI. We confirmed that interneuronal dysfunction in excitability is observed in brain slices upon current injections. However, we surprisingly found that network dynamics and interneuronal spiking were normal in the intact brain during ongoing activities, suggesting that additional cellular and network mechanisms may play a fundamental role in the pathogenesis of SMEI. These results contribute to unravel the basic mechanisms of SMEI pathogenesis and may represent an important step forward to the identification of new cellular targets for the pharmacological treatment of this intractable form of human epilepsy.

Authors' Contributions

A.M.D.S. and A.F. performed in vivo recordings. P.F. performed intracellular recordings in brain slices. I.M. and G.L. recorded and analyzed ictal events. D.V. performed optogenetic experiments in brain slices. A.M.D.S., P.F., I.M., S.C., S.P., D.V., and G.L. performed analysis. M.M. provided tools and reagents. A.B. and T.F. conceived and coordinated the project. G.C., A.B., and T.F. wrote the paper.

Funding

Notes

References

Adesnik H, Scanziani M. 2010. Lateral competition for cortical space by layer-specific horizontal circuits. Nature. 464:1155–1160.

Ascoli GA, Alonso-Nanclares L, Anderson SA, Barrionuevo G, Benavides-Piccione R, Burkhalter A, Buzsáki G, Cauli B, Defelipe J, Fairén A, et al. 2008. Petilla terminology: nomenclature of features of GABAergic interneurons of the cerebral cortex. Nat Rev Neurosci. 9:557–568.

Bacci A, Huguenard JR. 2006. Enhancement of spike-timing precision by autaptic transmission in neocortical inhibitory interneurons. Neuron. 49:119–130.

Beltramo R, D'Urso G, Dal Maschio M, Farisello P, Bovetti S, Clovis Y, Lassi G, Tucci V, De Pietri TD, Fellin T. 2013. Layer-specific excitatory circuits differentially control recurrent network dynamics in the neocortex. Nat Neurosci. 16:227–234.

Box GEP, Hunter JS, Hunter WG. 2005. Statistics for experimenters: design, innovation, and discovery. Hoboken, New Jersey: John Wiley & Sons.

Cammarota M, Losi G, Chiavegato A, Zonta M, Carmignoto G. 2013. Fast spiking interneuron control of seizure propagation in a cortical slice model of focal epilepsy. J Physiol. 591:807–822.

Cardin JA, Carlen M, Meletis K, Knoblich U, Zhang F, Deisseroth K, Tsai LH, Moore CI. 2009. Driving fast-spiking cells induces gamma rhythm and controls sensory responses. Nature. 459:663–667.

Cardin JA, Carlen M, Meletis K, Knoblich U, Zhang F, Deisseroth K, Tsai LH, Moore CI. 2010. Targeted optogenetic stimulation and recording of neurons in vivo using cell-type-specific expression of Channelrhodopsin-2. Nat Protoc. 5:247–254.

Carracedo LM, Kjeldsen H, Cunnington L, Jenkins A, Schofield I, Cunningham MO, Davies CH, Traub RD, Whittington MA. 2013. A neocortical delta rhythm facilitates reciprocal interlaminar interactions via nested theta rhythms. J Neurosci. 33:10750–10761.

Cheah CS, Yu FH, Westenbroek RE, Kalume FK, Oakley JC, Potter GB, Rubenstein JL, Catterall WA. 2012. Specific deletion of $Na_{V1.1}$ sodium channels in inhibitory interneurons causes seizures and premature death in a mouse model of Dravet syndrome. Proc Natl Acad Sci USA. 109:14646–14651.

Claes L, Del-Favero J, Ceulemans B, Lagae L, Van BC, De JP. 2001. De novo mutations in the sodium-channel gene SCN1A cause severe myoclonic epilepsy of infancy. Am J Hum Genet. 68:1327–1332.

Contreras D. 2004. Electrophysiological classes of neocortical neurons. Neural Netw. 17:633–646.

Crunelli V, Hughes SW. 2010. The slow (<1 Hz) rhythm of non-REM sleep: a dialogue between three cardinal oscillators. Nat Neurosci. 13:9–17.

David F, Schmiedt JT, Taylor HL, Orban G, Di GG, Uebele VN, Renger JJ, Lambert RC, Leresche N, Crunelli V. 2013. Essential thalamic contribution to slow waves of natural sleep. J Neurosci. 33:19599–19610.

DeFelipe J, López-Cruz PL, Benavides-Piccione R, Bielza C, Larrañaga P, Anderson S, Burkhalter A, Cauli B, Fairén A, Feldmeyer D, et al. 2013. New insights into the classification and nomenclature of cortical GABAergic interneurons. Nat Rev Neurosci. 14:202–216.

Deleuze C, Pazienti A, Bacci A. 2014. Autaptic self-inhibition of cortical GABAergic neurons: synaptic narcissism or useful introspection? Curr Opin Neurobiol. 26:64–71.

Dombeck DA, Khabbaz AN, Collman F, Adelman TL, Tank DW. 2007. Imaging large-scale neural activity with cellular resolution in awake, mobile mice. Neuron. 56:43–57.

Dravet C. 2000. Severe myoclonic epilepsy in infants and its related syndromes. Epilepsia. 41 (Suppl 9):7.

Dravet C, Bureau M, Oguni H, Fukuyama Y, Cokar O. 2005. Severe myoclonic epilepsy in infancy: Dravet syndrome. Adv Neurol. 95:71–102.

Dugue GP, Dumoulin A, Triller A, Dieudonne S. 2005. Target-dependent use of co-released inhibitory transmitters at central synapses. J Neurosci. 25:6490–6498.

Dutton SB, Sawyer NT, Kalume F, Jumbo-Lucioni P, Borges K, Catterall WA, Escayg A. 2011. Protective effect of the ketogenic diet in Scn1a mutant mice. Epilepsia. 52:2050–2056.

Feldmeyer D. 2012. Excitatory neuronal connectivity in the barrel cortex. Front Neuroanat. 6:24.

Freund TF, Katona I. 2007. Perisomatic inhibition. Neuron. 56:33–42.

Gomez-Gonzalo M, Losi G, Chiavegato A, Zonta M, Cammarota M, Brondi M, Vetri F, Uva L, Pozzan T, de Curtis M, et al. 2010. An excitatory loop with astrocytes contributes to drive neurons to seizure threshold. PLoS Biol. 8:e1000352.

Gu F, Hazra A, Aulakh A, Ziburkus J. 2014. Purinergic control of hippocampal circuit hyperexcitability in Dravet syndrome. Epilepsia. 55:245–255.

Han S, Tai C, Westenbroek RE, Yu FH, Cheah CS, Potter GB, Rubenstein JL, Scheuer T, de la Iglesia HO, Catterall WA. 2012. Autistic-like behaviour in $Scn1a^{+/-}$ mice and rescue by enhanced GABA-mediated neurotransmission. Nature. 489:385–390.

Harris KD, Mrsic-Flogel TD. 2013. Cortical connectivity and sensory coding. Nature. 503:51–58.

Hedrich UB, Liautard C, Kirschenbaum D, Pofahl M, Lavigne J, Liu Y, Theiss S, Slotta J, Escayg A, Dihne M, et al. 2014. Impaired action potential initiation in GABAergic interneurons causes hyperexcitable networks in an epileptic mouse model carrying a human Na(V)1.1 mutation. J Neurosci. 34:14874–14889.

Hu H, Gan J, Jonas P. 2014. Interneurons. Fast-spiking, parvalbumin(+) GABAergic interneurons: from cellular design to microcircuit function. Science. 345:1255263.

Isaacson JS, Scanziani M. 2011. How inhibition shapes cortical activity. Neuron. 72:231–243.

Le MC, Monyer H. 2013. GABAergic interneurons shape the functional maturation of the cortex. Neuron. 77:388–405.

Lewis DA, Fish KN, Arion D, Gonzalez-Burgos G. 2011. Perisomatic inhibition and cortical circuit dysfunction in schizophrenia. Curr Opin Neurobiol. 21:866–872.

Liautard C, Scalmani P, Carriero G, de CM, Franceschetti S, Mantegazza M. 2013. Hippocampal hyperexcitability and specific epileptiform activity in a mouse model of Dravet syndrome. Epilepsia. 54:1251–1261.

Logothetis NK. 2003. The underpinnings of the BOLD functional magnetic resonance imaging signal. J Neurosci. 23:3963–3971.

Losi G, Cammarota M, Chiavegato A, Gomez-Gonzalo M, Carmignoto G. 2010. A new experimental model of focal seizures in the entorhinal cortex. Epilepsia. 51:1493–1502.

Marder E. 2011. Variability, compensation, and modulation in neurons and circuits. Proc Natl Acad Sci USA. 108 (Suppl 3):15542–15548.

Marder E. 2012. Neuromodulation of neuronal circuits: back to the future. Neuron. 76:1–11.

Marin O. 2012. Interneuron dysfunction in psychiatric disorders. Nat Rev Neurosci. 13:107–120.

Massimini M, Huber R, Ferrarelli F, Hill S, Tononi G. 2004. The sleep slow oscillation as a traveling wave. J Neurosci. 24:6862–6870.

Meisler MH, Kearney JA. 2005. Sodium channel mutations in epilepsy and other neurological disorders. J Clin Invest. 115:2010–2017.

Metherate R, Cox CL, Ashe JH. 1992. Cellular bases of neocortical activation: modulation of neural oscillations by the

nucleus basalis and endogenous acetylcholine. J Neurosci. 12:4701–4711.

Mohajerani MH, McVea DA, Fingas M, Murphy TH. 2010. Mirrored bilateral slow-wave cortical activity within local circuits revealed by fast bihemispheric voltage-sensitive dye imaging in anesthetized and awake mice. J Neurosci. 30:3745–3751.

Ogiwara I, Miyamoto H, Morita N, Atapour N, Mazaki E, Inoue I, Takeuchi T, Itohara S, Yanagawa Y, Obata K, et al. 2007. Na$_{v1.1}$ localizes to axons of parvalbumin-positive inhibitory interneurons: a circuit basis for epileptic seizures in mice carrying an Scn1a gene mutation. J Neurosci. 27:5903–5914.

Ohmori I, Ouchida M, Ohtsuka Y, Oka E, Shimizu K. 2002. Significant correlation of the SCN1A mutations and severe myoclonic epilepsy in infancy. Biochem Biophys Res Commun. 295:17–23.

Petersen CC, Grinvald A, Sakmann B. 2003. Spatiotemporal dynamics of sensory responses in layer 2/3 of rat barrel cortex measured in vivo by voltage-sensitive dye imaging combined with whole-cell voltage recordings and neuron reconstructions. J Neurosci. 23:1298–1309.

Petersen CCH, Hahn TTG, Mehta M, Grinvald A, Sakmann B. 2003. Interaction of sensory responses with spontaneous depolarization in layer 2/3 barrel cortex. Proc Natl Acad Sci USA. 100:13638–13643.

Rubinstein M, Han S, Tai C, Westenbroek RE, Hunker A, Scheuer T, Catterall WA. 2015. Dissecting the phenotypes of Dravet syndrome by gene deletion. Brain. 138:2219–2233.

Rudy B, Fishell G, Lee S, Hjerling-Leffler J. 2011. Three groups of interneurons account for nearly 100% of neocortical GABAergic neurons. Dev Neurobiol. 71:45–61.

Sachidhanandam S, Sreenivasan V, Kyriakatos A, Kremer Y, Petersen CC. 2013. Membrane potential correlates of sensory perception in mouse barrel cortex. Nat Neurosci. 16:1671–1677.

Schuchmann S, Hauck S, Henning S, Gruters-Kieslich A, Vanhatalo S, Schmitz D, Kaila K. 2011. Respiratory alkalosis in children with febrile seizures. Epilepsia. 52:1949–1955.

Schuchmann S, Schmitz D, Rivera C, Vanhatalo S, Salmen B, Mackie K, Sipila ST, Voipio J, Kaila K. 2006. Experimental febrile seizures are precipitated by a hyperthermia-induced respiratory alkalosis. Nat Med. 12:817–823.

Sheroziya M, Timofeev I. 2014. Global intracellular slow-wave dynamics of the thalamocortical system. J Neurosci. 34:8875–8893.

Sohal VS, Zhang F, Yizhar O, Deisseroth K. 2009. Parvalbumin neurons and gamma rhythms enhance cortical circuit performance. Nature. 459:698–702.

Steriade M. 2006. Grouping of brain rhythms in corticothalamic systems. Neuroscience. 137:1087–1106.

Steriade M, Contreras D, Dossi RC, Nunez A. 1993. The slow (less-than-1 Hz) oscillation in reticular thalamic and thalamocortical neurons—scenario of sleep rhythm generation in interacting thalamic and neocortical networks. J Neurosci. 13:3284–3299.

Steriade M, Nunez A, Amzica F. 1993a. A novel slow (less-than-1 Hz) oscillation of neocortical neurons in-vivo—depolarizing and hyperpolarizing components. J Neurosci. 13:3252–3265.

Steriade M, Nunez A, Amzica F. 1993b. Intracellular analysis of relations between the slow (less-than-1 Hz) neocortical oscillation and other sleep rhythms of the electroencephalogram. J Neurosci. 13:3266–3283.

Tai C, Abe Y, Westenbroek RE, Scheuer T, Catterall WA. 2014. Impaired excitability of somatostatin- and parvalbumin-expressing cortical interneurons in a mouse model of Dravet syndrome. Proc Natl Acad Sci USA. 111:E3139–E3148.

Timofeev I, Grenier F, Steriade M. 2002. The role of chloride-dependent inhibition and the activity of fast-spiking neurons during cortical spike-wave electrographic seizures. Neuroscience. 114:1115–1132.

Tsai MS, Lee ML, Chang CY, Fan HH, Yu IS, Chen YT, You JY, Chen CY, Chang FC, Hsiao JH, et al. 2015. Functional and structural deficits of the dentate gyrus network coincide with emerging spontaneous seizures in an Scn1a mutant Dravet Syndrome model during development. Neurobiol Dis. 77:35–48.

Turrigiano GG, Nelson SB. 2004. Homeostatic plasticity in the developing nervous system. Nat Rev Neurosci. 5:97–107.

Uhlhaas PJ, Singer W. 2010. Abnormal neural oscillations and synchrony in schizophrenia. Nat Rev Neurosci. 11:100–113.

Yu FH, Mantegazza M, Westenbroek RE, Robbins CA, Kalume F, Burton KA, Spain WJ, McKnight GS, Scheuer T, Catterall WA. 2006. Reduced sodium current in GABAergic interneurons in a mouse model of severe myoclonic epilepsy in infancy. Nat Neurosci. 9:1142–1149.